Effects of reservoir operations on glacial turbidity in a hydroelectric reservoir

Daniel M. Robb[1*], Roger Pieters[1,2] and Gregory A. Lawrence[1]

[1*]Department of Civil Engineering, University of British Columbia, Vancouver, British Columbia, Canada.
[2]Department of Earth, Ocean and Atmospheric Sciences, University of British Columbia, Vancouver, British Columbia, Canada.

*Corresponding author. E-mail: drobb@eoas.ubc.ca

Abstract

Turbidity limits light availability in many glacier-fed lakes and reservoirs, with far-reaching ecological consequences. We use field observations and hydrodynamic modelling to examine the physical processes affecting turbidity in the epilimnion of a glacier-fed hydroelectric reservoir in response to changes in reservoir operations (e.g. water level, inflows and withdrawals), and to natural processes (e.g. particle settling, internal seiching and upwelling). The combination of cold inflows and deep outlets leads to plunging inflows and the isolation of the epilimnion; this isolation, along with particle settling, results in a remarkable clearing of the epilimnion during summer. We simulate a wide range of scenarios based on 46 years of historical flows. We find that the water level and inflow rate in spring control epilimnetic turbidity at the beginning of summer, and this turbidity is a primary determinant of the turbidity and light penetration for the rest of the summer. Turbidity during summer is also impacted by wind-driven thermocline motions. We examine these motions using wave characteristics diagrams and two-dimensional spectra and identify the period and wavelength of the two dominant wave modes: the fundamental internal seiche ($\approx$ 4 days) and diurnally-forced waves. Occasionally, internal motions are large enough to upwell turbid metalimnetic water to the free surface at the upstream end of the reservoir. These upwelling events coincide with peaks in the inverse of the Wedderburn number. Pulses of upwelled water are advected downstream, setting up a longitudinal turbidity gradient.

Keywords: turbidity, glacial inflow, particle settling, internal seiche, physical limnology, reservoir modelling

1 Introduction

Through the construction and operation of an estimated 500,000 reservoirs greater than one hectare [1], humans have dramatically altered the hydrology, particle fluxes and biogeochemistry in downstream rivers, lakes and reservoirs [2–4]. Worldwide, 48% of river volume is moderately to severely impacted by dams, and with dams currently planned or under construction, this fraction would increase to 93% [5]. With an increasing proportion of the world's freshwater affected by dams, understanding the environmental response to reservoir operations is critical to sustaining freshwater ecosystems [6].

Dammed reservoirs provide 30 – 40% of the world's irrigation water [7] and 17% of global electricity generation through hydropower [8], as well as drinking water, flood control and navigation routes. Despite these benefits,

there is a heightened awareness of their ecological and water quality impacts [9]. Various impacts have been studied, including the pathway of nutrients from plunging inflow to the euphotic zone [10–12]; changes in downstream nutrients [13], turbidity [14] and light [15]; and the effects on biological productivity of converting a lake into a reservoir [16]. Here we investigate the effects of reservoir operations on water quality, in particular the effects on turbidity dynamics within a glacier-fed reservoir.

Turbidity is an important indicator of water quality, notably in glaciated catchments where high turbidity from glacial meltwater can be the dominant factor influencing the underwater light climate [17]. Glacial turbidity impacts primary productivity [18], plankton community composition [19], filter-feeding organisms [20] and predator-prey dynamics [21].

In this study we address the following questions: (1) what are the physical processes, e.g. stratification, wind and inflows, that control glacial turbidity in a reservoir; (2) how do these processes interact to bring turbid water to the epilimnion; and (3) how do reservoir operations modify these processes? To address these questions we conducted a field and numerical study of Carpenter Reservoir, a long and narrow reservoir subject to regular winds and turbid inflows. We apply a hydrodynamic model to examine the effects of reservoir operations on turbidity using 46 years of hydrological data in conjunction with field measurements collected from May to October in 2015 and 2016 [22].

2 Methods

2.1 Study site

Carpenter Reservoir ($50°51'$ N, $122°30'$ W) is part of the Bridge River hydroelectric complex, located $\sim$200 km north of Vancouver, British Columbia, Canada (Fig. 1a). The reservoir is located in a drowned river valley formed from the Bridge River by the construction of Terzaghi Dam in 1960, giving a water body that is long ($\sim$50 km) and narrow ($\sim$1 km), with a maximum surface area of 46 km^2 and a maximum depth of 50 m (Fig. 1b). The reservoir is fast flushing, with a bulk residence time of four months at full pool and typically less than one month during low water level in spring. Inflows into the reservoir contain high concentrations of fine glacial particles, which are slow to settle, and which give the water a characteristic cloudy (turbid) appearance. There is concern that glacial meltwater is limiting light penetration within the reservoir, reducing algal growth, and, in turn, decreasing fisheries productivity.

The vast majority of the water in Carpenter Reservoir is diverted through twin tunnels to Seton Lake, with an elevation drop of $\sim$400 m used for generating hydroelectricity. A small amount of water is released through low-level outlets at Terzaghi Dam to the Lower Bridge River to maintain a minimum environmental flow (Fig. 1a). Note, all the outlets are from the deepest part of the reservoir (Fig. 1c).

The diversion of water from Carpenter Reservoir to Seton Lake is the main component of the Bridge River hydroelectric complex operated by BC Hydro, the principal distributor of electricity in the province of British Columbia, Canada. The complex is BC Hydro's third largest with a maximum generating capacity of 492 MW,

accounting for 6 – 8% of the province's electrical supply. As a result, changes in reservoir operation have important economic consequences.

Construction of Terzaghi Dam blocked the upstream passage of anadromous salmon, and steelhead, significantly reducing returns to the Bridge River from the Fraser River (Fig. 1a). The confluence of the two rivers was one of the most important indigenous fishing sites in the Interior of British Columbia and continues to be of major cultural importance [23]. Carpenter Reservoir itself supports populations of kokanee (*Oncorhynchus nerka*), a landlocked sockeye salmon as well as sport fish such as rainbow trout (*Oncorhynchus mykiss*) and bull trout (*Salvelinus confluentus*), see Hirst [24].

2.2 Field data collection

From May to October of 2015 and 2016, measurements of physical and chemical properties were collected in Carpenter Reservoir. Monthly CTD (conductivity, temperature, depth) profiles were collected at up to nine locations along the reservoir using a profiler equipped with turbidity and photosynthetically active radiation (PAR) sensors. Monthly sampling of the major tributaries was conducted using a multi-parameter probe. From the same tributaries, continuous measurements of water temperature were recorded. In addition, continuous measurements of water temperature were recorded from temperature loggers attached to a mooring suspended from a log boom in the deepest part of the reservoir (Fig. 1b). Meteorological data were collected at two onshore stations along the reservoir (Fig. 1b). Further detail on the field data collection is provided in Robb et al. [22].

2.3 Hydrodynamic model

To help understand the physical processes influencing turbidity in Carpenter Reservoir, simulations were conducted using the two-dimensional laterally averaged hydrodynamic and water quality model, CE-QUAL-W2 version 3.72 [25]; see the Supplementary Information for further description of the model. This model captures the dynamics along the length of the reservoir while ensuring that the run time is modest, making it possible to explore a wide range of scenarios.

The model domain extended from the upstream end of Carpenter Reservoir to Terzaghi Dam. Model runs were initialized with the measured water temperature, turbidity and conductivity from the May CTD profile at Station C2 (Fig. 1b). The model was set up with inflows from La Joie Dam and the local drainage, and outflows to Seton Lake and the Lower Bridge River (Fig. 1a). Tributary inflows were represented as point discharges to the nearest horizontal segment and placed into the water column at the depth of neutral buoyancy.

Meteorological boundary conditions were driven by wind data from Five Mile Station located along the main fetch (MET1), and solar radiation, air temperature and relative humidity data collected on Terzaghi Dam (MET2, Fig. 1b). The model was run from spring to fall to simulate the biologically productive season. Simulations began on the date of the first sampling trip and ended on the date of the last sampling trip: 22 May 2015 to 20 October 2015 and 12 May 2016 to 14 October 2016.

First, the model was calibrated to, and validated against, the CTD profiles and mooring data collected in 2015 and 2016 (see the Supplementary Information). Next, the model was run using the historical inflows and

operational conditions from 1965 to 2017, excluding seven years with significant spill from Terzaghi Dam, for a total of 46 years. Over the life of the reservoir, it has been operated in a variety of ways in response to hydrological conditions (e.g. wet and dry years), variations in electricity demand, and changes in ecological constraints. To represent this variability, we ran the model driven by the inflows and outflows for each of the 46 years. These flows, along with the water level at the start of the model run, reproduced the water level for a given year. However, meteorological, profiler, and tributary sampling (temperature, conductivity and turbidity) data needed for the initial and boundary conditions, were only available for 2015 and 2016; these data were used to force the model for each of the 46 years, giving a total of 92 model runs.

Since meteorological and tributary sampling data were not available for the 46 years, these runs do not represent the water quality conditions during those years; rather, they represent a synthetic dataset generated using 46 years of measured flows subject to two sets of meteorological and tributary boundary conditions. While this is a limitation of the study, the variation in the flow over the years was significant. Subjecting various operational conditions to the same set of meteorological and tributary sampling data provided a basis for comparison between scenarios by removing the effects of interannual variability in the meteorological and tributary sampling data, thereby isolating the effects of reservoir operations. These model runs were used to identify those aspects of reservoir operations associated with extremes in epilimnetic turbidity.

2.4 Calculations

2.4.1 Light attenuation and turbidity

The measured turbidity averaged over the euphotic depth and the light attenuation coefficient computed from photosynthetically active radiation (PAR) profiles were highly correlated $\left(R^2 = 0.91\right)$, see Robb et al. [22]. The regression enabled the parameterization of the diffuse light attenuation coefficient, K_d, as a linear function of turbidity, Tu, namely, $K_d = a + bTu$, where $a = 0.185$ m^{-1} gives the light attenuation due to water without particles, and $b = 0.081$ m^{-1} NTU^{-1} represents the light attenuation due to suspended particles measured as turbidity. This relationship between turbidity and light attenuation is similar to those reported for other glacier-fed water bodies [17, 26, 27].

2.4.2 Euphotic depth

The euphotic depth, h_{eu}, is the depth where the light intensity, I, is reduced to 1% of that just below the water surface, I_0. The rate of change of I with depth, z, is given by

$$\frac{\mathrm{d}I}{\mathrm{d}z} = -K_d I, \tag{1}$$

where K_d is the diffuse attenuation coefficient [28]. For the simplest case of a constant K_d, the solution to Eq. 1 is $I(z) = I_0 \exp(-K_d z)$, giving a euphotic depth of

$$h_{\mathrm{eu}} = \frac{\ln(100)}{K_d}. \tag{2}$$

However, in Carpenter Reservoir, K_d is not a constant; it is strongly correlated with turbidity [22], which, in turn, varies with distance along the reservoir, x, with depth, z, and with time, t. For a given x and t, the euphotic depth can be written implicitly as

$$\int_0^{h_{\mathrm{eu}}} K_d\left(x,z,t\right)\mathrm{d}z = \ln\left(100\right). \tag{3}$$

In the hydrodynamic model, the euphotic depth, $h_{\mathrm{eu}}\left(x,t\right)$, was computed from the simulated turbidity, $Tu\left(x,z,t\right)$, by converting Tu to K_d and vertically integrating K_d from the water surface to the depth where light intensity declined to 1% of the surface value.

2.4.3 Particle settling

To estimate the rate of particle settling out of the epilimnion, we apply the approach of Smith [29], Reynolds [30] and Tedford et al. [31]:

$$Tu_E\left(t\right) = Tu_{E_0}\exp\left(-\frac{t}{\tau}\right), \tag{4}$$

where Tu_E is the turbidity of the epilimnion, Tu_{E_0} is the initial turbidity of the epilimnion, $\tau = h_1/w_s$ is the e-folding timescale, representing the time required for the turbidity of the epilimnion to decrease by a factor of $1/e$, where h_1 is the depth of the epilimnion, and w_s is the particle settling velocity.

2.4.4 Basin-scale internal seiches

For two-layer stratification, the fundamental internal seiche period, T_1, and the phase speed, c_p, can be approximated by the Merian formula:

$$T_1 = \frac{2L}{c_p} \quad \text{and} \quad c_p = \sqrt{g'\frac{h_1 h_2}{h_1+h_2}}, \tag{5}$$

where L and h_1 are the length and depth of the epilimnion, respectively; we take h_2 as the volume-weighted average depth of the hypolimnion, and $g' = g\left(\rho_2-\rho_1\right)/\rho_2$ is the reduced gravity associated with the density difference across the interface, where ρ_1 and ρ_2 refer to the densities of the epilimnion and hypolimnion, respectively.

2.4.5 Wedderburn number

To determine the effect of wind forcing on basin-scale internal motion, we compute the Wedderburn number, $W = g'h_1^2/(u_*^2 L)$, a measure of the interfacial deflection relative to the depth of the undisturbed interface [32], where $u_* = \sqrt{(\rho_a/\rho_w)C_D U_W^2}$ is the wind shear velocity [33], where ρ_a is the density of air, ρ_w is the density of water, C_D is the drag coefficient between air and the water surface, and U_W is the wind speed. For $W \lesssim 1$, the interface reaches the free surface at the upwind end of the water body, resulting in upwelling of denser fluid into the epilimnion. For continuous profiles with a sharp density interface, partial upwelling is common for $W \lesssim 10$ [34, 35]. For $W \gtrsim 10$, the displacement of the interface is much smaller than the depth of the epilimnion. To

calculate W, the along-valley component of the wind stress was smoothed using a rolling-average filter with a window size equal to $T_1/4$ [36].

3 Results

In what follows, we examine the hydrological and meteorological observations used as model boundary conditions. We then look at the modelled seasonal stratification for 2015. The results for 2016 are shown in the Supplementary Information and are complementary to those for 2015. Finally, we present the 46 model scenarios driven by historical flows and describe their seasonal evolution.

3.1 Hydrological and meteorological observations

Inflows into Carpenter Reservoir originate from two main sources: the regulated inflow released from La Joie Dam (27%) and the unregulated inflow from the local tributaries (63%). In 2015, the inflow from La Joie Dam was relatively constant throughout the year, while the local inflow peaked during spring freshet (Fig. 2a). Outflow to Seton Lake was generally steady, and the outflow through Terzaghi Dam to the Lower Bridge River was low (Fig. 2b). The water level variation in 2015 was typical for a hydroelectric reservoir in Canada, low in April and filling during freshet (Fig. 2c).

From May to October, the temperature of the inflow from La Joie Dam was relatively steady, between 8 and 10 °C (Fig. 2d, red). By contrast, the temperature of the local inflow showed strong seasonal and diurnal variations (Fig. 2d, blue). Both the inflow from La Joie Dam and from the local inflow were cooler than the epilimnion (Fig. 2d, shades of red). Inflow from La Joie Dam (catchment 19% glaciated) was fresher and generally more turbid than inflow from the local tributaries (catchment $<2\%$ glaciated), see Fig. 2e,f. Note the high turbidity of the local inflow on 23 May 2015 may have bias, as samples were collected after a rainstorm the previous evening.

The wind over Carpenter Reservoir was channelized through the steep-sided valley, with the prevailing direction down-valley toward Terzaghi Dam (Fig. 1b, insets). The wind showed a strong diurnal pattern, rising in late morning, peaking in the afternoon and declining to $<1\,\mathrm{m\,s^{-1}}$ in the evening (Fig. 2g).

3.2 Model calibration

The model was calibrated by adjusting a small subset of parameters until the computed results best matched the field observations collected in 2015 and 2016. The first step was a comparison of the measured and modelled water temperature, followed by conductivity, and finally turbidity. The root mean square error (RMSE) between the modelled temperature, conductivity and turbidity and the CTD measurements for 2015 was 0.80 °C, 9.1 $\mu\mathrm{S\,cm^{-1}}$, and 5.7 NTU, respectively (with RMSE for turbidity in the epilimnion of 1.7 NTU). The RMSE between the modelled and moored temperature was 0.88 °C. This agreement is comparable to that reported in similar model studies [37–39]; see the Supplementary Information for detail.

3.3 Modelled seasonal stratification in 2015

The model provides a continuous time series not only of temperature, but also of conductivity and turbidity, and here we describe the seasonal evolution of all three at Station C2 near the dam. The simulated water temperature for 2015 illustrates the seasonal evolution of the thermocline as the epilimnion warmed in summer and then cooled and deepened in fall (Fig. 2h). There were times when the depth of the modelled thermocline oscillated over periods of 4 to 5 days due to wind-driven internal seiching. For example, wind from the west pushed the warm epilimnion toward Terzaghi Dam, deepening the epilimnion near the dam (15 July 2015, Fig. 2g,h), and when the wind subsided, the epilimnion near the dam became shallower again (17 July 2015, Fig. 2g,h). These temporal oscillations are shown as peaks and valleys at the thermocline in Fig. 2h.

From May to August 2015, the simulated turbidity of the epilimnion declined from 4 to 0.7 NTU, whereas turbidity in the deep water was much higher, dominated by tributary inflow which plunged to depth (Fig. 2i). In May and early June, plunging inflow to the hypolimnion was dominated by local tributaries with high turbidity (Fig. 2e). Toward the end of the model period, inflow from La Joie Dam dominated with a turbidity that rose steadily to nearly 100 NTU by October 2015 (Fig. 2e).

The simulated conductivity, C_{25}, of the epilimnion remained relatively high and steady through summer (90 – 100 $\mu S\,cm^{-1}$), illustrating the isolation of the epilimnion (Fig. 2j). The C_{25} of the epilimnion declined in fall as the surface layer was mixed down, and as deeper water — with lower C_{25} (60 – 70 $\mu S\,cm^{-1}$) — was mixed into the epilimnion. In the hypolimnion, the variation in C_{25} followed that of the inflows, with moderate C_{25} during freshet (May to early June), and decreasing C_{25} from July onward, reflecting the dominance of the inflow from La Joie Dam with lower C_{25} (Fig. 2a,f) and the short residence time of the hypolimnion (0.5 – 2 months, Robb et al. [22]). The modelled temperature, turbidity and C_{25} in 2016 exhibited similar seasonal evolution as in 2015 (see Fig. S9 in the Supplementary Information).

3.4 Longitudinal variations of epilimnetic turbidity in 2015

Having examined temperature, turbidity and conductivity near the dam (Station C2), we now examine the temporal variations in epilimnetic turbidity along the length of the reservoir (Fig. 3a). The turbidity was lower near the dam, increased away from the dam, and was higher near the upstream end of the reservoir, which was dominated by inflow. During downstream wind events, the epilimnion tilted downward towards the dam, and the metalimnion upwelled near the inflow. The wind then transported this metalimnetic fluid downstream at the water surface, seen as pulses of turbidity in Fig. 3a. When the wind subsided, the fronts of turbid fluid retreated.

The Wedderburn number, W, represents the ability of the wind to induce upwelling, with more upwelling at low W. It is notable how well the modelled upwelling events coincide with peaks in the inverse of the measured Wedderburn number (Fig. 3a). The higher spatiotemporal resolution offered by the model has enabled us to capture the strong connection between the Wedderburn number, wind-driven upwelling, the turbidity flux into the epilimnion, and the resulting gradient in epilimnetic turbidity along the length of the reservoir.

The measured and modelled turbidities of the epilimnion are plotted in Fig. 3b at two stations at either end of the reservoir. Turbidity was high at the upwind end of the reservoir (Station C9) since this was where wind-driven upwelling occured. The turbidity at Station C9 was also highly variable since the upwelling-affected region was advected upstream and downstream of the station in response to variations in wind and basin-scale seiching. Particles settled out of the epilimnion as they were transported downwind, resulting in a longitudinal reduction in turbidity. Consequently, the turbidity at the downwind end (Station C2) was typically much lower than at the upwind end (Station C9). During summer, when the epilimnion was relatively isolated, turbidity declined at both stations, and particle settling was the dominant process driving changes in epilimnetic turbidity, with wind-driven upwelling and longitudinal dispersion playing a secondary role [22]. In fall, surface mixed layer deepening entrained turbid water from the hypolimnion into the epilimnion and led to rapid increases in turbidity throughout the epilimnion (Fig. 3a).

The modelled turbidity at Stations C2 and C9 are in good agreement with the monthly measurements, except in fall at Station C2 (Fig. 3b). In fall, weak stratification makes the rate of surface mixed layer deepening especially sensitive to the along-reservoir wind field (insets, Fig. 1b). That is, a small difference between the true wind over the water body and the wind forcing imposed by the model can lead to a large difference in the rate of deepening, with an associated large difference in turbidity flux into the epilimnion.

3.5 Modelled scenarios driven by historical flows (1965 – 2017)

Here we examine the link between reservoir operations and epilimnetic turbidity variations by simulating the reservoir hydrodynamics using the inflows and outflows from 1965 to 2017, in conjunction with the meteorology and tributary sampling data collected in 2015. The simulated turbidity of the epilimnion for these years is shown in Fig. 4c. Each line represents the time variation of turbidity at 1 m depth at Station C2 near the dam. The coloured lines indicate selected years when turbidity was high (1999, 2017), close to average (2011) and low (2015), while the grey lines mark the remaining years. Using the data collected in 2016 gave similar results (see Figs. S12 and S13).

The epilimnetic turbidity of Carpenter Reservoir varied seasonally. Turbidity was high in spring when the reservoir was weakly stratified and susceptible to wind-driven mixing. During summer, the reservoir stratification increased, and particle settling was the dominant process affecting turbidity except during the occasional wind-storm. The turbidity increased in fall as the surface mixed layer deepened, entraining turbid water from below. Note that the model runs which began with low water levels (1999 and 2017, Fig. 4b) also showed large increases in turbidity in spring (Fig. 4c). By contrast, in the model run with high initial water level (2015, Fig. 4b), the turbidity declined steadily from the start of the model run until fall. During summer, the turbidity of the epilimnion varied by up to an order of magnitude between scenarios, depending on the reservoir operations and hydrological conditions (Fig. 4c).

These model results illustrate several physical processes that drive changes in epilimnetic turbidity in Carpenter Reservoir, including particle settling, wind forcing and convective cooling. By examining the time series data in

Fig. 4, four regimes were identified. Spring was characterized by periods of calm (Regime I) resulting in gradual declines in turbidity, alternating with wind events (Regime II) leading to rapid increases in turbidity (Fig. 4a,c). In summer, particle settling led to a decline in turbidity from a maximum at the beginning of summer. However, the decline was interrupted by wind events, coinciding with small, short-lived increases in turbidity or with reduced settling rates (settling dominant, wind modified; Regime III). In fall, wind (Regime II) and convective cooling (Regime IV) were important; with weakening stratification, wind and cooling resulted in episodic increases in turbidity or reduced rates of settling.

3.5.1 Spring

Relationship between epilimnetic turbidity and residence time in spring. In some model runs, the stratification in spring isolated the epilimnion, while in others — with low water level and high inflow — the stratification was too weak to suppress mixing, leading to the transport of turbid water into the epilimnion. The strong relationship between the bulk residence time during spring, t_r, and epilimnetic turbidity at the beginning of summer, Tu^*, is shown in Fig. 5. Here we define Tu^* as the turbidity at Station C2 at 1 m depth at the beginning of summer (chosen here to be 20 June), and $t_r = \bar{V}/\bar{Q}_{\text{in}}$, where V is the volume of water in the reservoir, Q_{in} is the total inflow, and the overbar denotes a time average from the beginning of the model run to the beginning of summer (22 May – 20 June). The results are insensitive to the exact definitions of Tu^* and t_r. For low t_r ($\lesssim 25$ days), Tu^* generally decreases as t_r increases, whereas, for high t_r ($\gtrsim 25$ days), Tu^* is low (< 2 NTU) and insensitive to t_r (Fig. 5). In the following, we examine the variation of epilimnetic turbidity in Carpenter Reservoir in spring, summer and fall using the model results driven by historical flows.

We will illustrate the interaction of the various processes affecting turbidity during spring by looking at four model runs (2015, 2011, 2017 and 1999) that follow a progression from least to most turbid surface waters, corresponding to a progression from high to low residence times (Table 1). The mixing in spring has biological significance because it sets the turbidity at the beginning of summer, which, in turn, controls the epilimnetic turbidity and underwater light conditions for the duration of summer (Fig. 4c).

During spring, there were three periods of calm (Regime I), alternating with three periods of wind (Regime II), see Fig. 4c. During the periods of calm, the surface waters experienced a gradual decrease in turbidity due to particle settling, whereas during the periods of wind the turbidity in the surface water increased in some years and declined in others (Fig. 4a,c). We now examine the response of the turbidity in the reservoir to these periods of calm and wind.

Spring 2015. We begin by examining the model run for the spring of 2015, which is representative of years with long residence times (Fig. 5). During periods of calm, the epilimnion returned to its undisturbed position (Fig. 6b,d,f), and turbidity declined due to particle settling (Fig. 4a,c). During the periods of wind, the epilimnion tilted down toward the dam (Fig. 6c,e,g), but winds were too weak to transport significant quantities of turbid water into the epilimnion. Instead, turbidity at Station C2 continued to decline despite the windstorms (grey regions, Fig. 4a,c). The rate of decline was relatively insensitive to wind, as indicated by the nearly constant slope of the

Table 1 Spring reservoir volume, inflow, residence time and turbidity in selected years.

Year	Initial Volume[1]	Avg. Inflow[2] $\bar{Q}_{\text{in}}$	Avg. Volume[3] $\bar{V}$	Residence Time[4] t_r	End of Spring Turbidity[5] Tu^*
	(Mm^3)	($\text{m}^3\,\text{s}^{-1}$)	(Mm^3)	(days)	(NTU)
2015	380	220	560	32	1.8
2011	190	200	300	19	2.6
2017	60	240	200	10	9.0
1999	35	200	110	7.1	15

[1]Reservoir volume at the start of the model run (22 May)
[2]Time-averaged inflow from the beginning of the model run to the end of spring (22 May – 20 June)
[3]Time-averaged reservoir volume (22 May – 20 June)
[4]Residence time computed as the time-averaged volume divided by the time-averaged inflow (22 May – 20 June)
[5]Turbidity at Station C2 at 1 m depth at the end of spring (20 June)

solid blue line in Fig. 4c. Overall, in the 2015 model run, the spring period saw a decline in turbidity, and, as a result, summer began with an initial turbidity far lower than for most other model runs (Figs. 4c, 6g).

Spring 2011. The 2011 model run represents a case where wind led to increases in turbidity, but these were less than the decreases due to particle settling; the combined effect was a net decline in turbidity over the spring period (Figs. 4c, 6h–m). During the first two windstorms, turbidity followed the same pattern of decline as in 2015, as opposed to during the third windstorm (16 – 20 June) when turbidity increased (Fig. 4c).

Spring 2017. For the 2017 model run, turbidity at Station C2 responded to all three windstorms. On 28 May, just before the first windstorm, the reservoir volume was only 11% of capacity (Fig. 6n), and just one quarter of the reservoir volume as on the same day in 2015 (Fig. 6b). At this time, the reservoir was only 15 km long with the upstream 7 km dominated by inflows and the epilimnion extending the remaining 8 km to the dam wall (Fig. 6n). In the 2015 model run, by contrast, the reservoir was 35 km long with the upstream 5 km dominated by inflows and the epilimnion extending 30 km to the dam wall (Fig. 6b). In 2017, during the first windstorm (28 – 30 May), turbidity at Station C2 nearly doubled (Fig. 4c), and the wind pushed the surface water toward the dam, shortening and deepening the epilimnion (Fig. 6o). As the epilimnion deformed under wind stress, turbid water was mixed into the epilimnion, with a small daily jump in turbidity following the daily wind (28 – 30 May, Fig. 4a,c). This contrasts with 2015, when, over the same period, turbidity declined (Fig. 4c).

From 30 May to 5 June 2017, during a period of calm, the wind subsided and the epilimnion returned to its undisturbed position (Fig. 6p). Without wind stress to balance the pressure gradient set up by the previous windstorm, surface currents changed direction from downstream (toward the dam) to upstream. The region dominated by inflow retreated upstream at 3 $\text{km}\,\text{d}^{-1}$, roughly consistent with the baroclinic wave speed within the epilimnion, $c = \frac{1}{2}\sqrt{g' h_1} = 4.5\ \text{km}\,\text{d}^{-1}$. By 5 June, the turbidity at Station C2 had declined (Fig. 4c), but it remained higher than on the same date in the 2015 and 2011 model runs. For the remainder of spring, the turbidity responded in a similar manner, increasing during periods of wind and decreasing during the period of calm.

So far, increases in turbidity have resulted from two mechanisms. First, localized wind-driven epilimnetic deepening mixed turbid, metalimnetic fluid into the surface waters. In this case, turbidity responded within hours

of a wind impulse, often giving rise to jumps in turbidity (e.g. 5 June, 16 June; Fig. 4c). Second, surface wind-driven currents transported turbid water from the inflow-dominated region toward the downstream portion of the reservoir, driving an increase in turbidity at Station C2 (e.g. 6 – 10 June, 17 – 20 June; Fig. 4c). We now look at a third mechanism, where increases in turbidity are triggered by inflow.

Spring 1999. At the beginning of the 1999 model run, on 22 May, the reservoir was drawn down to a depth of 13 m and a volume of 35 Mm^3, just 3% of the reservoir volume at full pool, and an order of magnitude smaller than the volume on the same date in 2015 (Table 1). At this time, the inflow was $200\,m^3\,s^{-1}$, and the reservoir volume more than doubled by 25 May. On 25 May, nearly all the reservoir upstream of Station C2 was occupied by well-mixed inflow that had entered the reservoir since the beginning of the model run; that is, well-mixed riverine conditions extended close to Station C2. The rapid filling of the reservoir mixed turbid water into the epilimnion where turbidity nearly doubled on 25 May (Fig. 4c). Note that conditions during this day were calm, indicating that the mixing event leading to the increase in turbidity was triggered by inflow instead of wind-driven mixing.

As the reservoir filled further, subsequent jumps in turbidity at Station C2 coincided with windstorms, following the pattern of the 2017 model run (Fig. 4c). Note that after the first windstorm (28 – 30 May), the turbidity at Station C2 in the 1999 model run increased to ∼30 NTU, comparable to that of the inflow (Fig. 4c).

3.5.2 Summer

After summer began on 20 June, particle settling became the primary driver of turbidity variations with wind playing a secondary role. Here we begin by looking at particle settling and then wind-driven seiching.

The turbidity of the epilimnion during summer was characterized by an approximately exponential decline. For example, during the first 30 days of summer (20 June – 20 July) in the 2015 model run, turbidity at Station C2 at 1 m depth declined with an e-folding time of $\tau \approx 48$ d (Fig. 4c). During this period, the modelled (and observed) epilimnion depth was ∼8.5 m, corresponding to an effective particle settling velocity of $w_s^{\text{eff}} = 0.18\ \text{m}\,\text{d}^{-1}$. This value is close to the settling velocity specified in the model, $w_s = 0.2\ \text{m}\,\text{d}^{-1}$ (blue dashed line, Fig. 4c), confirming that particle settling is a dominant driver of turbidity variations during summer. Note that $w_s^{\text{eff}} < w_s$, because small turbidity fluxes entering the epilimnion opposed the turbidity fluxes leaving the epilimnion due to settling. For example, during the first 30 days of summer, conditions were relatively calm, and turbidity declined by 2.0% per day (Fig. 4c). By contrast, during the next 30 days, winds were stronger — they imparted ∼70% more energy to the water surface — and turbidity declined by only 1.2% per day. Several other factors may also have contributed to the reduced effective settling rate such as weakened stratification (allowing increased turbidity flux into the epilimnion), increased thermocline depth, and the increasing difference in turbidity between the hypolimnion and epilimnion.

The wind also caused internal motions in the predominantly two-layer structure, namely motions along the thermocline separating the warm epilimnion from the cooler hypolimnion. For much of the summer, the thermocline followed the 17 °C isotherm, and we chose this isotherm as a representative depth of the thermocline; other choices gave similar results. To illustrate the displacement of the thermocline, we plot the 17 °C isotherm from 20

June to 02 September after which time the epilimnion began to cool rapidly and surface mixed layer deepening ensued (Fig. 7).

The thermocline oscillated with two dominant periods. First, basin-scale oscillations with a period of approximately four days are evident in the wave characteristics plots for each of our selected years (2015, 2011, 2017 and 1999), e.g. green lines in Fig. 7e. For 20 June to 02 September, the Merian formula (Eq. 5) gives $c_p \approx 19 \pm 2\,\mathrm{km\,d^{-1}}$ and $T_1 \approx 4.1 \pm 0.6$ d, consistent with the values of c_p and T_1 obtained from the wave characteristics (Fig. 7). The second oscillatory period corresponds to the diurnal wind forcing. The prevailing wind blows down valley in the afternoon, resulting in a series of daily wind impulses. With each impulse, a depression of the thermocline was generated at the dam, which propagated upstream toward the inflow-dominated region (e.g. blue lines, Fig. 7e). The upstream propagating wave then reflected off the inflow and traveled back downstream (e.g. red lines, Fig. 7e). The inverse slope of the lines gives $c_p \approx 18\,\mathrm{km\,d^{-1}}$, consistent with our estimate using Eq. 5.

The two-dimensional spectra of the thermocline oscillations are shown in Fig. 8. There are distinct peaks in the spectra at period $T_f = 1$ d and wavelength $\lambda = 18$ km corresponding to the daily wind forcing. At the period of $T_1 \approx 4.1$ d, corresponding to the fundamental basin-scale seiche, there is a broader band reflecting the changes in stratification and water level over the summer. Also shown are the lines corresponding to $c_p = 19\,\mathrm{km\,d^{-1}}$, as predicted using the Merian formula (Eq. 5), and consistent with our estimates based on the plot of wave characteristics (Fig. 7).

The response of the thermocline in all four model years was similar (Fig. 7); this is not surprising given that the wind forcing was the same for all model years shown. However, there remain differences between the years due to changes in stratification and water level. There were also changes within a given year, for example in early July 1999, low L and high g' resulted in a shorter than average basin-scale seiche period (3.8 d, magenta lines), compared with late August 1999 when it was longer (4.5 d, green lines), see Fig. 7e.

3.5.3 Fall

In fall, there were three periods of wind followed by periods of calm (Fig. 4a). During the wind events the epilimnion deepened, and the epilimnetic turbidity increased due to the entrainment of higher turbidity water from the hypolimnion (Fig. 4c). During the periods of calm, epilimnetic turbidity increased due to penetrative convection and decreased due to particle settling. Overall, during fall, epilimnetic turbidity increased substantially in all model runs (Fig. 4c).

4 Discussion

4.1 Physical processes

While there are a variety of factors that can influence water quality in a reservoir, we have examined one such factor: turbidity. We have investigated the physical processes that determine the epilimnetic turbidity within a reservoir. The model results indicated that the average residence time during spring was the primary control of turbidity in the epilimnion at the beginning of summer (Fig. 5), and that the turbidity at the end of spring controlled

the turbidity for the rest of the summer (Fig. 4). That is, simulations with low water level and high inflows in spring led to high turbidity in summer, and simulations with high water level and low inflows in spring led to low turbidity in summer.

During spring, the key physical process was the interaction between inflow and the existing volume of water within the reservoir. When the volume in the reservoir was large, then emerging spring stratification isolated the near surface from the turbid plunging inflow. When the volume of the reservoir was small, the inflow overwhelmed the water in the reservoir and delayed stratification as in the 1999 model run (Fig. 6t).

During summer, the key physical processes were plunging inflows, wind-driven upwelling, internal motions, longitudinal dispersion and particle settling, which interacted to transport turbid fluid into, out of, and within the epilimnion (Fig. 3). Wind events in combination with basin-scale internal seiches upwelled small pulses of turbid fluid from the hypolimnion at the upstream end of the reservoir into the epilimnion (Fig. 7). The upwelled fluid set up a longitudinal gradient in turbidity in the epilimnion (Fig. 3a). As the summer progressed, suspended particles settled out of the epilimnion, which led to a decline in epilimnetic turbidity (Fig. 4c).

In summer, the epilimnion was relatively isolated, primarily receiving small fluxes of turbid water from upwelling at the upwind end of the reservoir. These fluxes into the epilimnion were smaller than the fluxes out of the epilimnion due to particle settling. The turbidity of the epilimnion at the beginning of summer was the primary factor determining the turbidity for the rest of the summer. When the initial turbidity was high, then it remained high; when the initial turbidity was low, then it remained low. In all cases, the particle settling flux dominated the mass balance, which led to an overall decline in turbidity over the summer.

During fall, surface mixed layer deepening was the dominant process, entraining turbid water from the metalimnion into the epilimnion, which led to a rapid increase in epilimnetic turbidity (Figs. 3 and 4c). During this period, weak stratification made the rate of surface mixed layer deepening especially sensitive to wind. For example, even a single wind event could cause enough surface mixed layer deepening to significantly increase the turbidity of the epilimnion (Figs. 3b and 4a,c). We now discuss some of the implications of the physical processes described above.

4.2 Implications for the euphotic zone

In Carpenter Reservoir, as in many glacier-fed water bodies [17], turbidity controls the volume of the euphotic zone. During summer, a remarkable contrast between epilimnetic and hypolimnetic turbidity developed due to stratification and the settling of particles. By late summer, epilimnetic turbidity declined to 0.5 – 3 NTU (Fig. 4c), whereas hypolimnetic turbidity remained elevated, ranging from 5 – 30 NTU (e.g. Fig. 2i). This contrast has important implications. For example, for a turbidity of 1 NTU ($K_d = 0.27$ m^{-1}), Eq. 2 predicts a euphotic depth of $\sim$17 m. However, the epilimnion was shallower than this, typically $\sim$8 m, and the presence of more turbid water below the epilimnion means that light passing through the epilimnion is rapidly attenuated just below the epilimnion. As a result, the summer euphotic zone generally ended close to the top of the turbid hypolimnion. The euphotic depth followed the oscillations of the thermocline in response to wind (Fig. 2i).

4.3 Implications for water quality

It is common to have water quality criteria based on turbidity. A useful metric is to evaluate the volume of water in a lake or reservoir, V_{WQ}, that satisfies a particular water quality requirement. Here we define V_{WQ} as the volume of the reservoir with a turbidity less than 5 NTU; we chose this value since turbidity exceeding this threshold can limit primary production in glacial lakes [40] and interfere with filter-feeding in cladocerans [20], a key food source for kokanee (*Oncorhynchus nerka*). Note the turbidity of the inflow into Carpenter Reservoir was always greater than 5 NTU (Fig. 4c), meaning that under well-mixed conditions V_{WQ} would equal zero. However, thermal stratification and particle settling resulted in a much lower turbidity in the surface layer than at depth. In all model runs, the decline in summer epilimnetic turbidity led to an increase in V_{WQ}, reaching a maximum in late summer and early fall (Fig. 4d), followed by a rapid decline in fall as the surface mixed layer deepened. For model runs with high epilimnetic turbidity at the beginning of summer (1999, 2017 and six others), V_{WQ} remained equal to zero well into the summer, which has implications of, for example, a shorter biologically productive season. A similar criterion could be applied to systems where other water quality parameters are a concern, for example, contaminants [41] or nutrients [11].

4.4 Effects of wind and thermocline deflections

Even though the simulated internal motions were similar from year to year, the light climate differed. For example, the contour marking $Tu = 5$ NTU at the water surface is shown in Fig. 7; surface waters upstream (downstream) of this contour have turbidity greater (less) than 5 NTU. At the beginning of summer in 2015, surface turbidity greater than 5 NTU occurred in the inflow-affected region while the entire epilimnion was less than 5 NTU. By contrast, in the early summer of 1999, the entire surface of the reservoir was greater than 5 NTU. As the summer of 1999 progressed, a turbidity of less than 5 NTU first occurred near the dam on 10 July; this can also be seen in Fig. 4d where the volume of the reservoir with a turbidity less than 5 NTU was zero until 10 July. After this date, the epilimnion progressively cleared due to particle settling.

Carpenter Reservoir experiences diurnal down-valley winds originating from the Bridge Glacier [42] and common to many mountainous regions [43]. Our model results have shown how these winds can result in upwelling and transport of turbid water into the epilimnion, as well as significant motion of the thermocline at both the diurnal and fundamental seiche periods. In addition to turbidity, internal motions can enhance photosynthesis by circulating phytoplankton through a nonlinear light field [44], can stress fish experiencing large temperature fluctuations [45], and can transport nutrients to the euphotic zone enhancing algae growth [10].

4.5 Implications for the Bridge River and other systems

Starting in 2016, the hydroelectric utility decided to lower the water level in Downton Reservoir, upstream of Carpenter Reservoir, to reduce the seismic risk of the ageing La Joie Dam (Fig. 1a). Keeping the water level low in Downton Reservoir resulted in abnormally high inflows into Carpenter Reservoir, which led to high outflows to the Lower Bridge River and to Seton Lake in 2016 (Fig. S9b). To accommodate these high flows into Carpenter

Reservoir, the hydroelectric utility also lowered water levels in Carpenter Reservoir beginning in 2017 (Fig. 4b). The model results suggest that low water level and high flushing rates in spring contributed to higher turbidity in the epilimnion during these years (Figs. 4b,c and 5). The water level regime in subsequent years, 2018 – 2022, was similar to that in 2017 and will likely be representative of future conditions until anticipated repairs are completed.

The Bridge Glacier above the upstream Downton Reservoir (Fig. 1a) is undergoing significant retreat [46]. In recent decades, this has already reduced late summer streamflow by ∼10% [47], and it is expected to increase the temperature of the meltwater at the headwaters of the Bridge River [48]. While the effect of these changes on Carpenter Reservoir will be moderated by flow through Downton Reservoir, we anticipate that years with lower late summer inflow will become more prevalent. This also highlights the importance of continued collection of tributary temperature and turbidity data, as the present study relied on only two years of observations.

Prior to the construction of the twin diversion tunnels, there was no connection between Carpenter Reservoir and Seton Lake [49], see Fig. 1a. The turbid discharge from the hypolimnion of Carpenter Reservoir to the surface of Seton Lake has reduced the euphotic depth of Seton Lake in summer, from approximately 20 m to 10 m [50].

The behaviour of Carpenter Reservoir highlights the consequences of the main feature of reservoirs, that the reservoir volume is often subject to dramatic variation. For example, in temperate latitudes, reservoirs are typically drawn down by early spring to allow for storage of freshet inflow. Our work demonstrates that the combination of low reservoir volume and a high flux of turbid inflow can impact the reservoir stratification in spring and ultimately the turbidity during summer.

In summary, using hydrodynamic modelling and field observations, we investigated the physical processes affecting epilimnetic turbidity and the role of reservoir operations in modifying these processes. By simulating a range of scenarios based on 46 years of historical flows, subject to two sets of meteorological conditions, we found that, during summer, the combination of cold inflows, deep withdrawals and strong thermal stratification resulted in the isolation of, and subsequent particle settling from, the epilimnion in all 92 model scenarios. However, despite these similarities, the turbidity of the epilimnion during summer varied by up to an order of magnitude between scenarios, depending on the reservoir operations and hydrological conditions, particularly in spring.

The results presented in this paper are applicable to a range of natural and constructed water bodies where the fate of turbid inflows has important impacts on water quality. They will also inform water use planning for Carpenter Reservoir, which aims to balance a suite of reservoir functions including hydropower generation, aquatic ecosystem services, and cultural significance. Possible future research includes examining the effect of warmer inflows into Carpenter Reservoir due to glacier loss [48] and investigating the effect of releases from Carpenter Reservoir on turbidity in the downstream Seton Lake [50].

Supplementary information. The online version contains supplementary material.

Acknowledgments. We are grateful to St'át'imc Nation for allowing us to conduct fieldwork within their traditional territory. Funding and support were provided by BC Hydro, Limnotek Research and Development Inc., and St'át'imc Eco-Resources (SER) Ltd. Funding was also provided by the Natural Sciences and Engineering Research Council (NSERC) of Canada through the CRD, CGS and USRA programs. We thank Bonnie Adolf, Gilda Davis,

and Jude Manahan of SER who managed the study as part of a larger water use planning project. Special thanks goes to Chris Perrin of Limnotek Research for the opportunity to collaborate on this project and for many discussions on all parts of this work. Access to BC Hydro field facilities was provided by Dorian Turner. Field support was provided by crews servicing concurrent projects in the Bridge River system: support included Allison Hebert and Shannon Harris of BC Ministry of Environment and Climate Change Strategy; Dani Ramos and Annika Putt of Instream Fisheries Research Ltd.; and Tyler Creasey and Jessica Hopkins of SER. Marc Laynes and Jeff Sneep are thanked for boat and field support. We are grateful to Shauna Bennett for data management. Odin Scholz (Split Rock Environmental Ltd.) and Brad Oleman (BC Ministry of Forests Lands and Natural Resource Operations) are thanked for support on access to meteorological data from the Five Mile Forest Service weather station. We also thank Thea Rodgers and Melanie Mewhort, who assisted with instrument service and data analysis and whose salaries were subsidized by the UBC Work Learn program.

Conflict of interest. The authors declare that they have no conflict of interest.

Author contributions. DMR and RP conceived the numerical experiments. RP designed the observational study. DMR and RP contributed to field data collection. DMR conducted the data analysis and numerical modelling. DMR wrote the manuscript with contributions from RP and GAL. All authors approved the final submitted manuscript.

References

[1] Downing, J.A., Prairie, Y.T., Cole, J.J., Duarte, C.M., Tranvik, L.J., Striegl, R.G., McDowell, W.H., Kortelainen, P., Caraco, N.F., Melack, J.M., Middelburg, J.J.: The global abundance and size distribution of lakes, ponds, and impoundments. Limnol. Oceanogr. **51**(5), 2388–2397 (2006) https://doi.org/10.4319/lo.2006.51.5.2388

[2] Friedl, G., Wüest, A.: Disrupting biogeochemical cycles - Consequences of damming. Aquat. Sci. **64**(1), 55–65 (2002) https://doi.org/10.1007/s00027-002-8054-0

[3] Vörösmarty, C.J., Meybeck, M., Fekete, B., Sharma, K., Green, P., Syvitski, J.P.M.: Anthropogenic sediment retention: major global impact from registered river impoundments. Glob. Planet. Change **39**(1-2), 169–190 (2003) https://doi.org/10.1016/s0921-8181(03)00023-7

[4] Maavara, T., Chen, Q., Meter, K.V., Brown, L.E., Zhang, J., Ni, J., Zarfl, C.: River dam impacts on biogeochemical cycling. Nat. Rev. Earth Environ. **1**, 103–116 (2020) https://doi.org/10.1038/s43017-019-0019-0

[5] Grill, G., Lehner, B., Lumsdon, A.E., MacDonald, G.K., Zarfl, C., Liermann, C.R.: An index-based framework for assessing patterns and trends in river fragmentation and flow regulation by global dams at multiple scales. Environ. Res. Lett. **10**(1), 015001 (2015) https://doi.org/10.1088/1748-9326/10/1/015001

[6] Poff, N.L., Schmidt, J.C.: How dams can go with the flow. Science **353**(6304), 1099–1100 (2016) https://doi.org/10.1126/science.aah4926

[7] Yoshikawa, S., Cho, J., Yamada, H.G., Hanasaki, N., Kanae, S.: An assessment of global net irrigation water requirements from various water supply sources to sustain irrigation: rivers and reservoirs (1960–2050). Hydrol. Earth Syst. Sci. **18**(10), 4289–4310 (2014) https://doi.org/10.5194/hess-18-4289-2014

[8] REN21: Renewables 2021 Global Status Report. Technical report, REN21 Secretariat, Paris, France (2021)

[9] Vörösmarty, C.J., McIntyre, P.B., Gessner, M.O., Dudgeon, D., Prusevich, A., Green, P., Glidden, S., Bunn, S.E., Sullivan, C.A., Liermann, C.R., Davies, P.M.: Global threats to human water security and river biodiversity. Nature **467**(7315), 555–561 (2010) https://doi.org/10.1038/nature09440

[10] Fischer, H.B., Smith, R.D.: Observations of transport to surface waters from a plunging inflow to Lake Mead. Limnol. Oceanogr. **28**(2), 258–272 (1983) https://doi.org/10.4319/lo.1983.28.2.0258

[11] Rueda, F.J., Fleenor, W.E., Vicente, I.d.: Pathways of river nutrients towards the euphotic zone in a deep-reservoir of small size: Uncertainty analysis. Ecol. Model. **202**(3-4), 345–361 (2007) https://doi.org/10.1016/j.ecolmodel.2006.11.006

[12] Pieters, R., Lawrence, G.A.: Plunging inflows and the summer photic zone in reservoirs. Water Qual. Res. J. Can. **47**(3-4), 268–275 (2012) https://doi.org/10.2166/wqrjc.2012.143

[13] Ashley, K., Thompson, L.C., Lasenby, D.C., McEachern, L., Smokorowski, K.E., Sebastian, D.: Restoration of an Interior Lake Ecosystem: the Kootenay Lake Fertilization Experiment. Water Qual. Res. J. Can. **32**(2), 295–324 (1997) https://doi.org/10.2166/wqrj.1997.021

[14] Finger, D., Schmid, M., Wüest, A.: Effects of upstream hydropower operation on riverine particle transport and turbidity in downstream lakes. Water Resour. Res. **42**(8), 08429 (2006) https://doi.org/10.1029/2005wr004751

[15] Jaun, L., Finger, D., Zeh, M., Schurter, M., Wüest, A.: Effects of upstream hydropower operation and oligotrophication on the light regime of a turbid peri-alpine lake. Aquat. Sci. **69**(2), 212–226 (2007) https://doi.org/10.1007/s00027-007-0876-3

[16] Matzinger, A., Pieters, R., Ashley, K.I., Lawrence, G.A., Wüest, A.: Effects of impoundment on nutrient availability and productivity in lakes. Limnol. Oceanogr. **52**(6), 2629–2640 (2007) https://doi.org/10.4319/lo.2007.52.6.2629

[17] Rose, K.C., Hamilton, D.P., Williamson, C.E., McBride, C.G., Fischer, J.M., Olson, M.H., Saros, J.E., Allan, M.G., Cabrol, N.: Light attenuation characteristics of glacially-fed lakes. J. Geophys. Res. Biogeo. **119**(7), 1446–1457 (2014) https://doi.org/10.1002/2014jg002674

[18] Slemmons, K.E.H., Saros, J.E., Simon, K.: The influence of glacial meltwater on alpine aquatic ecosystems: a review. Environ. Sci. Proc. Imp. **15**(10), 1794–1806 (2013) https://doi.org/10.1039/c3em00243h

[19] Sommaruga, R.: When glaciers and ice sheets melt: consequences for planktonic organisms. J. Plankton Res. **37**(3), 509–518 (2015) https://doi.org/10.1093/plankt/fbv027

[20] Koenings, J.P., Burkett, R.D., Edmundson, J.M.: The Exclusion of Limnetic Cladocera from Turbid Glacier-Meltwater Lakes. Ecology **71**(1), 57–67 (1990) https://doi.org/10.2307/1940247

[21] Jönsson, M., Ranåker, L., Nicolle, A., Ljungberg, P., Fagerberg, T., Hylander, S., Jephson, T., Lebret, K., Einem, J.v., Hansson, L.-A., Nilsson, P.A., Balseiro, E., Modenutti, B.: Glacial clay affects foraging performance in a Patagonian fish and cladoceran. Hydrobiologia **663**(1), 101–108 (2011) https://doi.org/10.1007/s10750-010-0557-4

[22] Robb, D.M., Pieters, R., Lawrence, G.A.: Fate of turbid glacial inflows in a hydroelectric reservoir. Environ. Fluid Mech. **21**, 1201–1225 (2021) https://doi.org/10.1007/s10652-021-09815-4

[23] Hayden, B.: A Complex Culture of the British Columbia Plateau: Traditional Stl'atl'imx Resource Use. UBC Press, Vancouver, British Columbia (1992)

[24] Hirst, S.M.: Impacts of the operation of existing hydroelectric developments on fishery resources in British Columbia. Inland fisheries. Can. Manuscr. Rep. Fish. Aquat. Sci. 2093. Technical report (1991)

[25] Cole, T.M., Wells, S.A.: CE-QUAL-W2: A two-dimensional, laterally averaged, hydrodynamic and water quality model, version 3.72. Technical report, Department of Civil and Environmental Engineering, Portland State University, Portland, Oregon (2015)

[26] Lloyd, D.S., Koenings, J.P., Laperriere, J.D.: Effects of Turbidity in Fresh Waters of Alaska. N. Am. J. Fish Manage. **7**(1), 18–33 (1987) https://doi.org/10.1577/1548-8659(1987)7⟨18:eotifw⟩2.0.co;2

[27] Koenings, J.P., Edmundson, J.A.: Secchi disk and photometer estimates of light regimes in Alaskan lakes: Effects of yellow color and turbidity. Limnol. Oceanogr. **36**(1), 91–105 (1991) https://doi.org/10.4319/lo.1991.36.1.0091

[28] Kirk, J.T.O.: Light and Photosynthesis in Aquatic Ecosystems. Cambridge University Press, Cambridge (1994)

[29] Smith, I.R.: A simple theory of algal deposition. Freshwater Biol. **12**(5), 445–449 (1982) https://doi.org/10.1111/j.1365-2427.1982.tb00639.x

[30] Reynolds, C.S.: The Ecology of Freshwater Phytoplankton. Cambridge University Press, Cambridge (1984)

[31] Tedford, E., Halferdahl, G., Pieters, R., Lawrence, G.A.: Temporal variations in turbidity in an oil sands pit

lake. Environ. Fluid Mech. **19**, 457–473 (2019) https://doi.org/10.1007/s10652-018-9632-6

[32] Imberger, J., Hamblin, P.F.: Dynamics of Lakes, Reservoirs, and Cooling Ponds. Annual Review of Fluid Mechanics **14**(1), 153–187 (1982) https://doi.org/10.1146/annurev.fl.14.010182.001101

[33] Fischer, H.B., List, J.E., Koh, C.R., Imberger, J., Brooks, N.H.: Mixing in Inland and Coastal Waters. Academic press, London (1979)

[34] Monismith, S.G.: An experimental study of the upwelling response of stratified reservoirs to surface shear stress. Journal of Fluid Mechanics **171**(-1), 407–439 (1986) https://doi.org/10.1017/s0022112086001507

[35] Monismith, S.G., MacIntyre, S.: The surface mixed layer in lakes and reservoirs. In: Likens, G.E. (ed.) Encyclopedia of Inland Waters, pp. 636–650. Academic Press, Oxford (2009). https://doi.org/10.1016/B978-012370626-3.00078-8

[36] Stevens, C., Imberger, J.: The initial response of a stratified lake to a surface shear stress. Journal of Fluid Mechanics **312**, 39–66 (1996) https://doi.org/10.1017/s0022112096001917

[37] Sullivan, A.B., Rounds, S.A., Sobieszczyk, S., Bragg, H.M.: Modeling hydrodynamics, water temperature, and suspended sediment in Detroit Lake, Oregon. Technical report, U. S. Geological Survey (2007)

[38] Gelda, R.K., King, A.T., Effler, S.W., Schweitzer, S.A., Cowen, E.A.: Testing and application of a two-dimensional hydrothermal/transport model for a long, deep, and narrow lake with moderate Burger number. Inland Waters **5**(4), 387–402 (2015) https://doi.org/10.5268/iw-5.4.804

[39] Kobler, U.G., Wüest, A., Schmid, M.: Effects of Lake–Reservoir Pumped-Storage Operations on Temperature and Water Quality. Sustainability **10**(6), 1968 (2018) https://doi.org/10.3390/su10061968

[40] Edmundson, J.A., Koenings, J.P.: The Effects of Glacial Silt On Primary Production, Through Altered Light Regimes and Phosphorus Levels, No. 68. Technical report (1986)

[41] Knauer, K., Nepf, H., Hemond, H.: The production of chemical heterogeneity in upper mystic lake. Limnology and Oceanography **45**(7), 1647–1654 (2000)

[42] Shea, J.M., Moore, R.D.: Prediction of spatially distributed regional-scale fields of air temperature and vapor pressure over mountain glaciers. J. Geophys. Res. Atmos. **115**, 23107 (2010) https://doi.org/10.1029/2010jd014351

[43] Oerlemans, J., Grisogono, B.: Glacier winds and parameterisation of the related surface heat fluxes. Tellus A **54**(5), 440–452 (2002) https://doi.org/10.3402/tellusa.v54i5.12164

[44] Evans, M.A., MacIntyre, S., Kling, G.W.: Internal wave effects on photosynthesis: Experiments, theory, and modeling. Limnol. Oceanogr. **53**(1), 339–353 (2008) https://doi.org/10.4319/lo.2008.53.1.0339

[45] Laval, B.E., Morrison, J., Potts, D.J., Carmack, E.C., Vagle, S., James, C., McLaughlin, F.A., Foreman, M.: Wind-driven summertime upwelling in a fjord-type lake and its impact on downstream river conditions: Quesnel Lake and River, British Columbia, Canada. Journal of Great Lakes Research **34**(1), 189–203 (2008)

[46] Chernos, M., Koppes, M., Moore, R.D.: Ablation from calving and surface melt at lake-terminating Bridge Glacier, British Columbia, 1984–2013. Cryosphere **10**(1), 87–102 (2016) https://doi.org/10.5194/tc-10-87-2016

[47] Moyer, A.N., Moore, R.D., Koppes, M.N.: Streamflow response to the rapid retreat of a lake-calving glacier. Hydrol. Process. **30**(20), 3650–3665 (2016) https://doi.org/10.1002/hyp.10890

[48] Bird, L.A., Moyer, A.N., Moore, R.D., Koppes, M.: Hydrology and thermal regime of an ice-contact proglacial lake: implications for stream temperature and lake evaporation. Hydrol. Process. **36**, 14566 (2022) https://doi.org/10.1002/hyp.14566

[49] Geen, G.H., Andrew, F.J.: Limnological changes in Seton Lake resulting from hydroelectric diversions. Technical report (1961)

[50] Barouillet, C., Cumming, B.F., Laird, K.R., Perrin, C.J., Selbie, D.T.: Influence of glacial flour on the primary and secondary production of Sockeye Salmon nursery lakes: a comparative modern and paleolimnological study. Can. J. Fish. Aquat. Sci. **76**, 2303–2314 (2019) https://doi.org/10.1139/cjfas-2018-0372

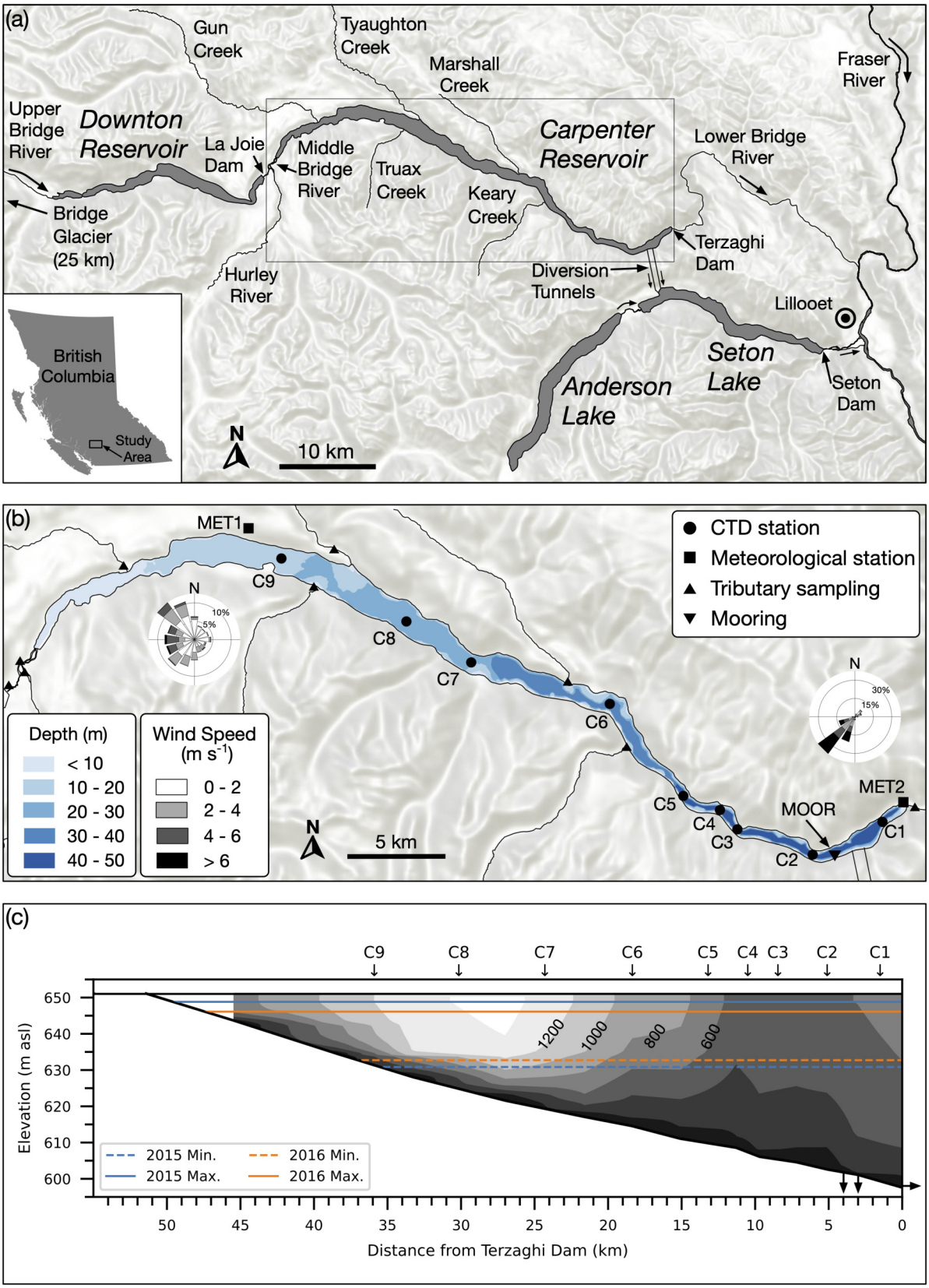

Fig. 1 (a) Map of the study area and (b) plan view of Carpenter Reservoir and monitoring stations. The box in (a) marks the location of panel (b). In (b), the contours indicate the depth of water below full pool (651.08 m asl). Wind roses are shown for Five Mile Station (MET1) and Terzaghi Dam (MET2). The major tributaries flowing into Carpenter Reservoir are shown as solid lines. (c) Profile view of Carpenter Reservoir showing the minimum and maximum water level in 2015 and 2016, and showing contours of reservoir width at 200-m intervals from 200 to 1400 m. CTD stations are marked C1–C9. The downward arrows at the reservoir bottom mark the twin tunnels to Seton Lake. The rightward arrow at the dam marks the outflow to the Lower Bridge River.

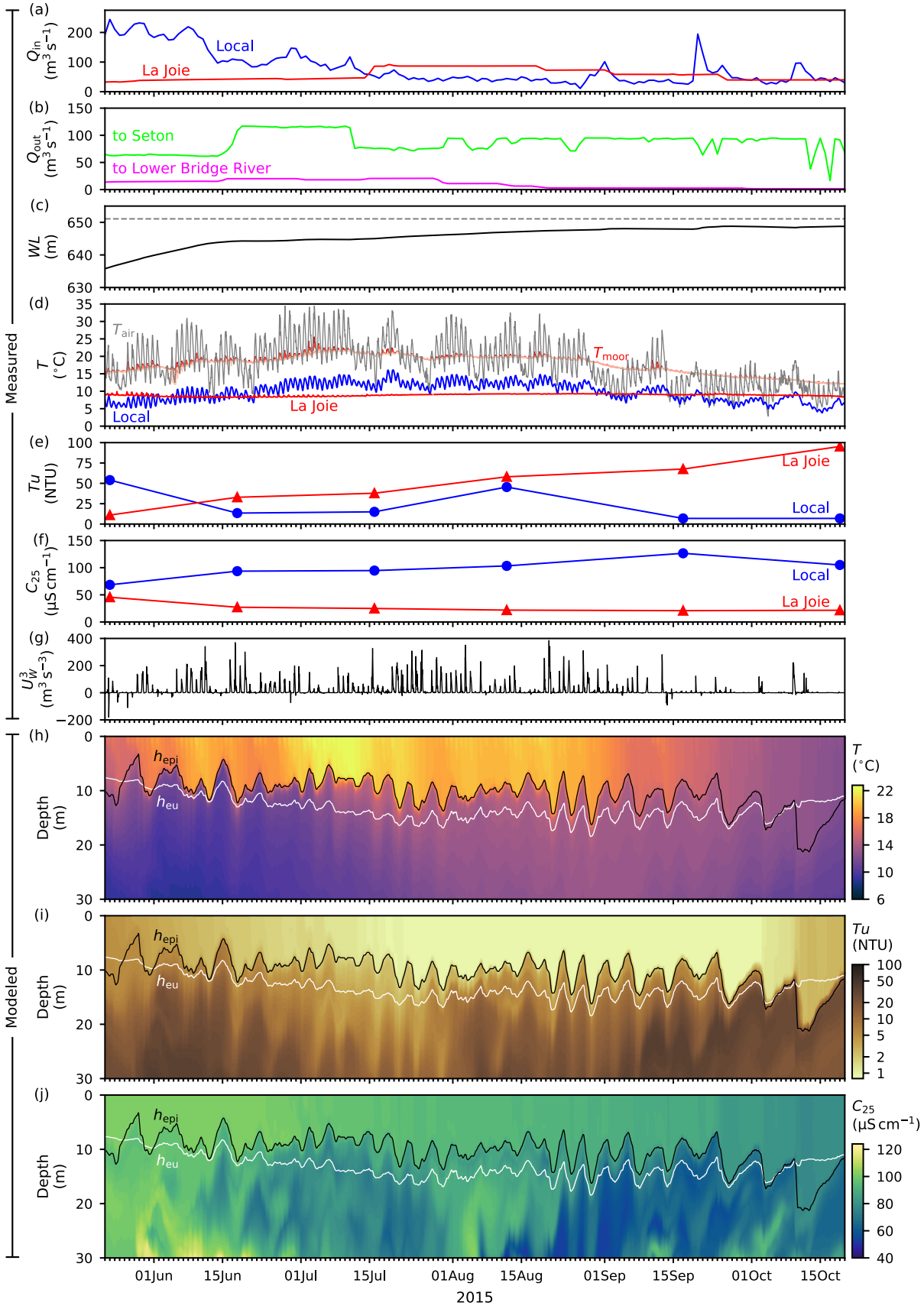

Fig. 2 Measured (a) inflows, (b) outflows, (c) water level, (d–f) flow-weighted tributary temperature, turbidity and conductivity, (g) along-axis wind speed cubed; and modelled (h–j) temperature, turbidity and conductivity, at Station C2, 22 May to 20 October 2015. In (c), the dashed line marks full pool (651.08 m asl). In (d), air temperature and mooring temperature (0–5 m) are shown in grey and shades of red, respectively. In (g), positive wind is from the west toward the dam. In (h–j), the black line marks the epilimnion depth (maximum temperature gradient) and the white line the euphotic depth.

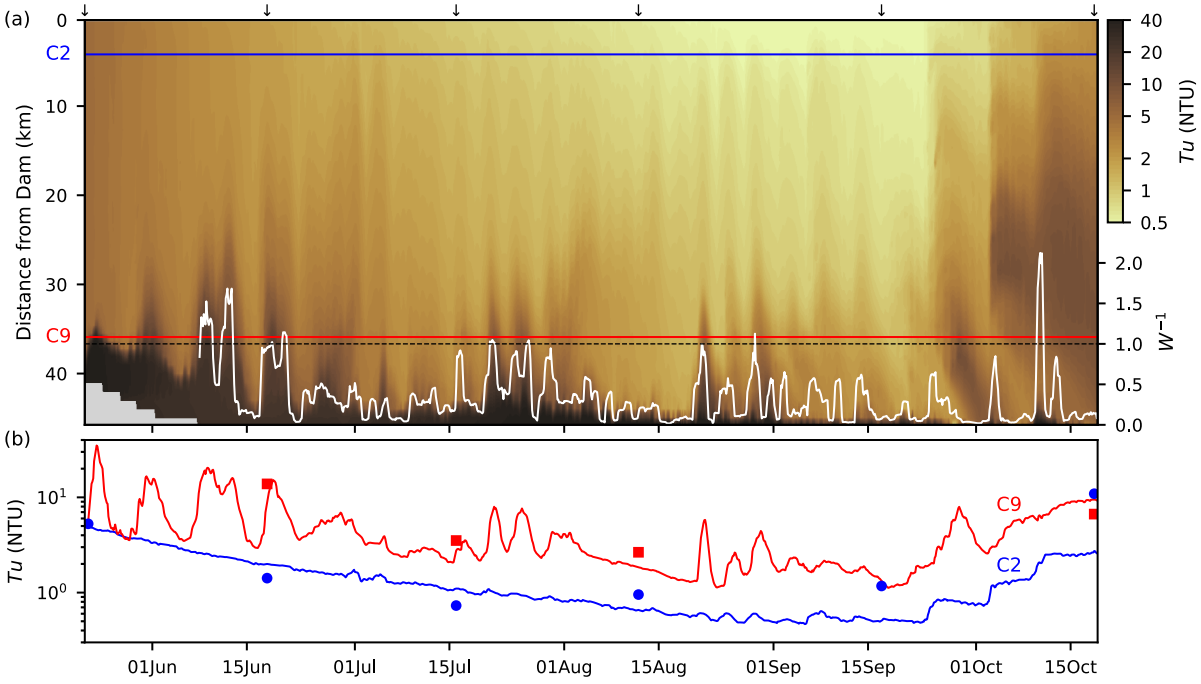

Fig. 3 (a) Modelled turbidity at 1 m depth representative of the epilimnion (contours), and the inverse of the measured Wedderburn number during summer stratification (white line), 22 May – 20 October 2015. (b) Measured and modelled turbidity at 1 m depth at Stations C2 (blue) and C9 (red). In (a), the solid horizontal lines mark the location of Stations C2 and C9, the dashed horizontal line marks $W = 1$, and the downward arrows indicate the survey dates. In (b), the markers indicate field measurements, and the lines indicate model results.

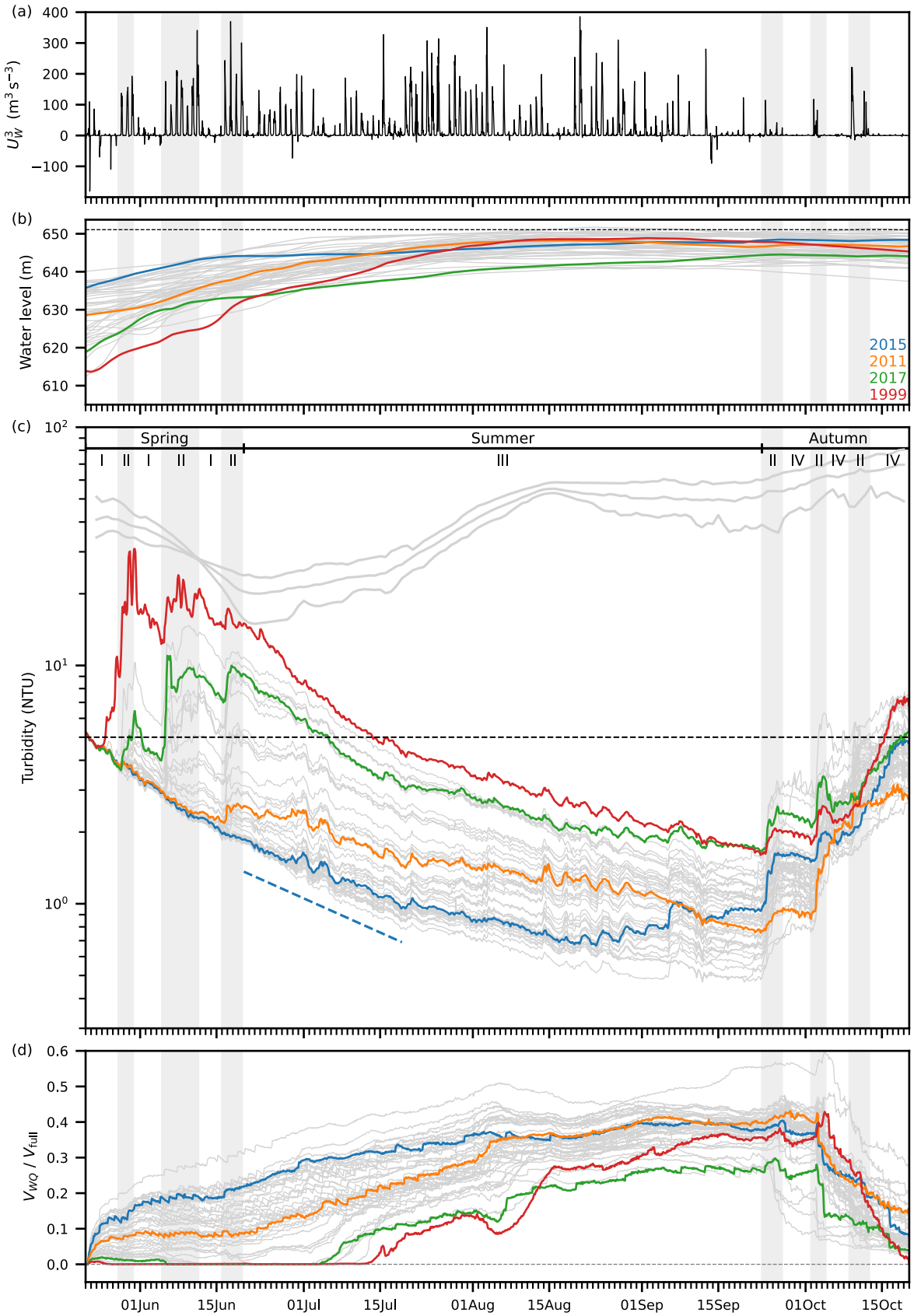

Fig. 4 Time series of (a) observed along-axis wind speed cubed, and (b) simulated reservoir water level, (c) simulated turbidity at Station C2 at 1 m depth, and (d) simulated volume of the reservoir with a turbidity less than 5 NTU, V_{WQ}, divided by the reservoir volume at full pool, V_{full}, (651.08m asl, 1.0×10^9 m^3). In (a), positive wind speed is from the west toward the dam. In (b), the dashed line marks the elevation of full pool. In (c), the blue dashed lined shows Eq. 4 for $w_s = 0.2$ m d^{-1} and $h_1 = 8.5$ m. In (b–d), the thin grey lines show the model results for all years 1965 – 2017, and the coloured lines show selected years. In (c), the thick grey lines show the flow-weighted turbidity of the inflows (median, 5$^{\mathrm{th}}$ and 95$^{\mathrm{th}}$ percentile). All model runs use the meteorological and tributary sampling data from 2015 (using 2016 gave similar results, see Fig. S12). Roman numerals mark Regimes described in the text.

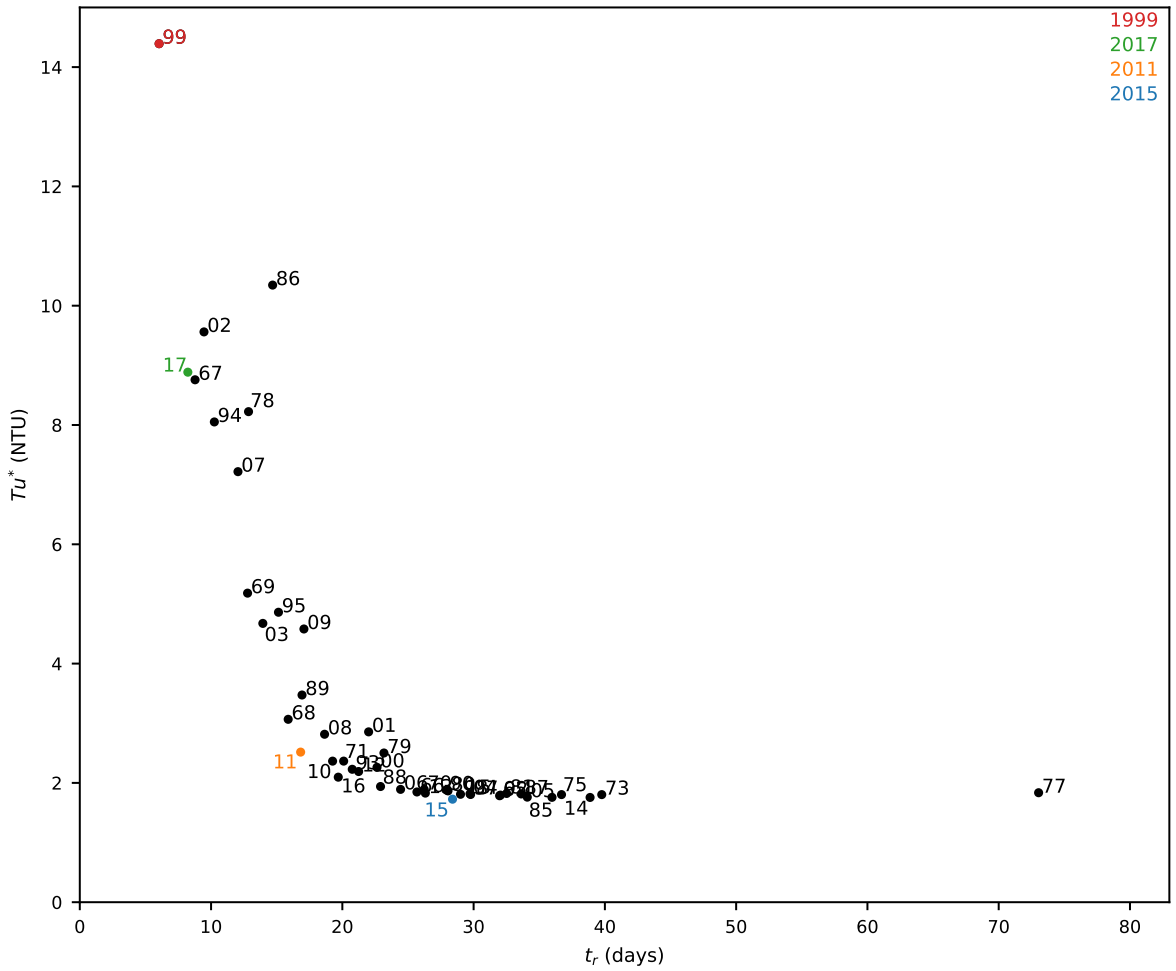

Fig. 5 Relationship between epilimnetic turbidity at Station C2 at 1 m depth at the beginning of summer, Tu^*, and the average residence time from the beginning of the model run to the beginning of summer, t_r, (22 May – 20 June). Shown are model runs (1965 – 2017) using the meteorological and tributary sampling data from 2015 (using 2016 gave similar results, see Fig. S13).

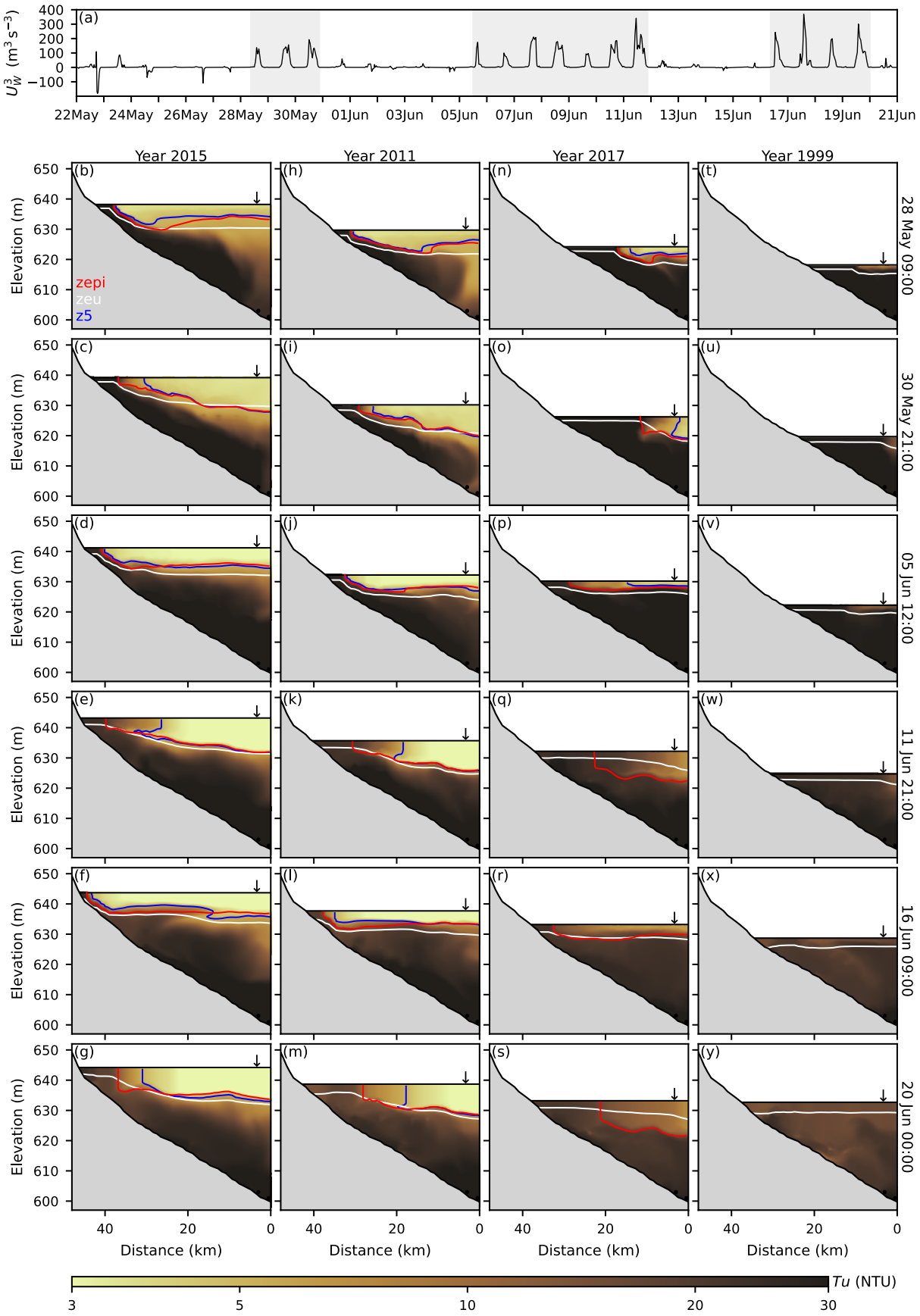

Fig. 6 Modelled turbidity before and after each wind event in spring. (a) Observed along-axis wind speed cubed and (b–y) snapshots of modelled turbidity for the 2015, 2011, 2017 and 1999 model runs during the spring period (22 May – 20 June). The white line marks the euphotic depth. The red line (if present) marks the thermocline depth. The blue line (if present) and the water surface bound the region where turbidity is less than 5 NTU. In (b–y), the downward arrow marks Station C2. The shading in (a) indicates the wind events in spring. The snapshots in (b–y) were taken at the beginning and end of each wind event. The times are indicated on the right-hand side of each row of snapshots.

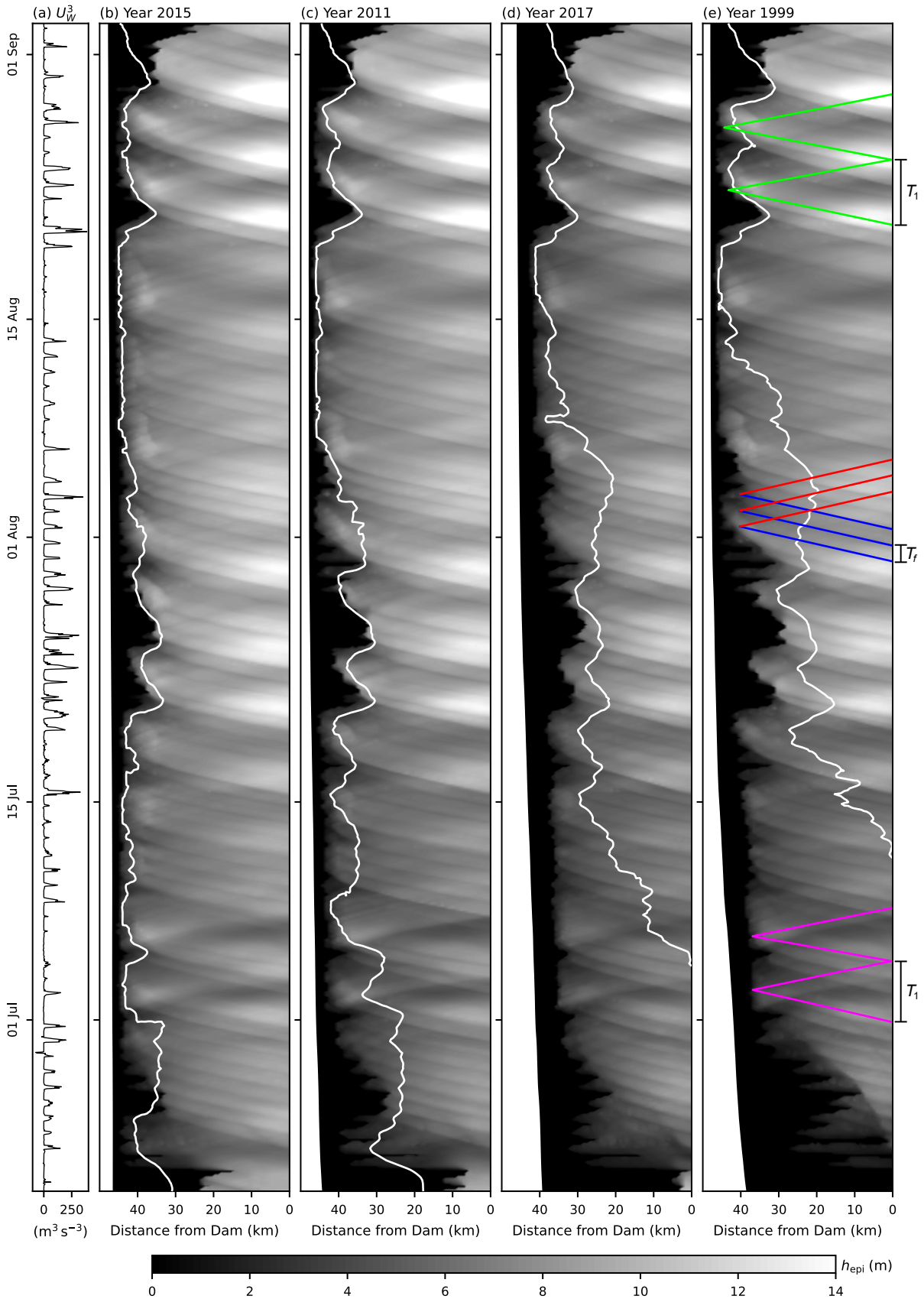

Fig. 7 (a) Along-axis wind speed cubed observed in 2015; positive wind is from the west toward the dam. (b–e) Wave characteristics plots of the modelled thermocline depth for the 2015, 2011, 2017 and 1999 model runs. The shading represents the depth of the thermocline below the water surface. The dark bands represent waves of elevation (crests), while light bands represent waves of depression (troughs). The phase velocity is given by the inverse slope of these bands: a more vertical band indicates a slower-moving wave, and a more horizontal band indicates a faster-moving wave. The white line indicates the 5 NTU contour at the water surface; the region bounded by the contour and the dam has a surface turbidity < 5 NTU. Recall that the meteorological forcing is the same for all model runs shown.

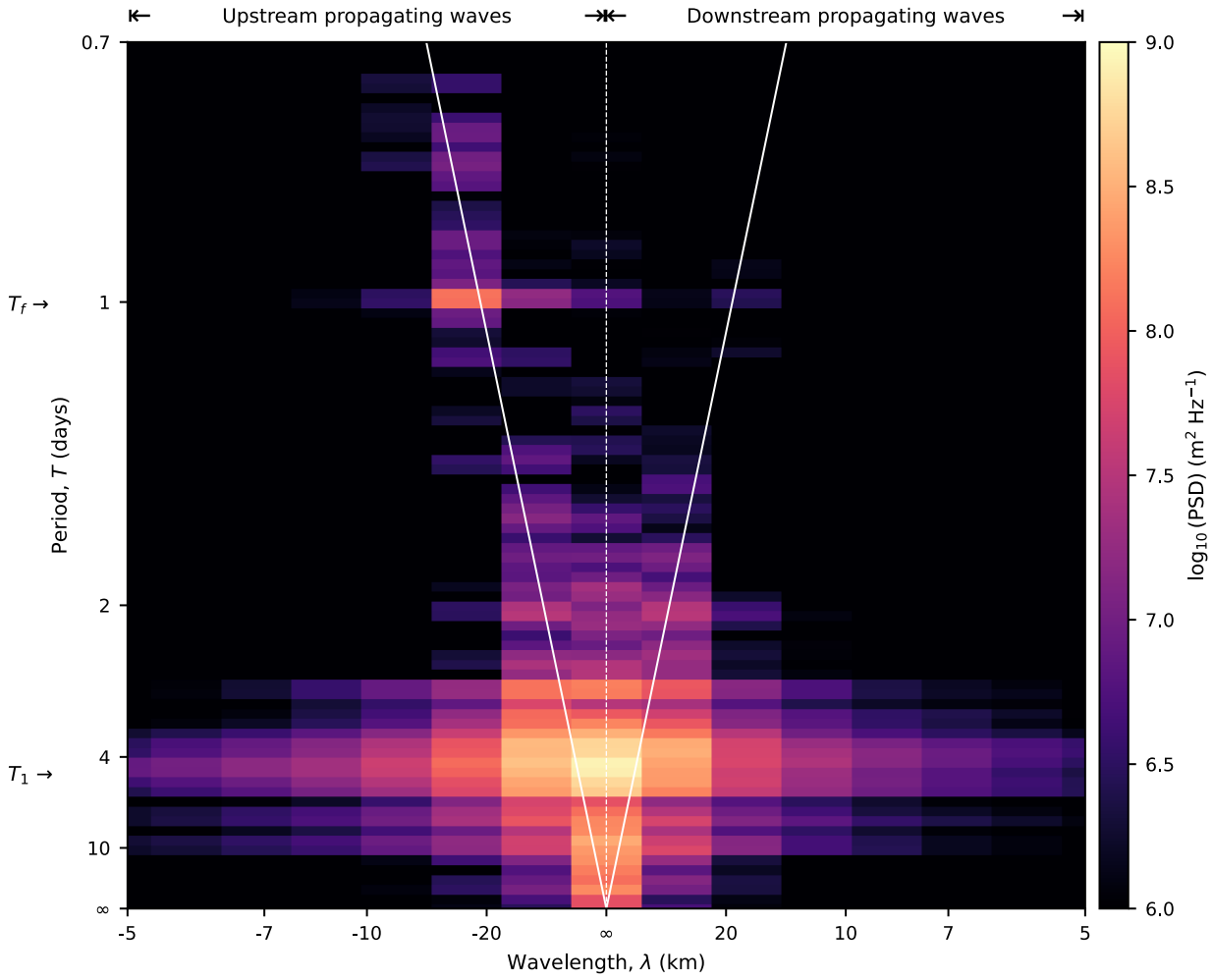

Fig. 8 Power spectral density (PSD) obtained by the two-dimensional Fourier transform of the modelled wave characteristics shown in Fig. 7b (the 2015 model run). Results for 2011, 2017, and 1999 are similar. The excited frequency band at 1 day corresponds to direct forcing by diurnal winds, T_f, and the broader band centered at 4.1 days corresponds to the fundamental internal seiche, T_1. Positive and negative wavelengths correspond to downstream and upstream propagating waves, respectively. The solid white lines correspond to the phase speed $c_p = 19$ km d^{-1} predicted using the Merian formula (Eq. 5).

Supplementary Information for

Effects of reservoir operations on glacial turbidity in a hydroelectric reservoir

Daniel M. Robb[1*], Roger Pieters[1,2] and Gregory A. Lawrence[1]

[1*]Department of Civil Engineering, University of British Columbia, Vancouver, British Columbia, Canada.

[2]Department of Earth, Ocean and Atmospheric Sciences, University of British Columbia, Vancouver, British Columbia, Canada.

*Corresponding author. E-mail: drobb@eoas.ubc.ca

S1 Hydrodynamic model

The model, CE-QUAL-W2, solves the unsteady Reynolds-averaged Navier-Stokes equations for conservation of mass and momentum under the Boussinesq approximation and the hydrostatic pressure assumption. In addition, advection-diffusion transport equations are solved for heat, dissolved solids (conductivity), suspended solids (turbidity), and passive tracers. The equations are solved in the longitudinal (x) and vertical (z) directions after laterally averaging in the transverse (y) direction. The governing equations are solved on a fixed rectangular grid using a z-level vertical coordinate system. The horizontal eddy diffusivity is assumed to be constant and is set equal to $1\ \mathrm{m^2\,s^{-1}}$, while the vertical eddy diffusivity varies in space and time and is computed using a k-ε turbulence closure scheme [1, 2]. The model has been successfully applied to a wide variety of applications, including the environmental response to pumped storage [3], internal seiching [4], and climate scenarios [5].

The model domain extended from the upstream end of Carpenter Reservoir to Terzaghi Dam and consisted of 56 horizontal segments along the length of the reservoir (Fig. S1a). Segment lengths varied from 700 to 1000 m, and each segment was divided into vertical layers regularly spaced at 0.5-m intervals (Fig. S1b). Model runs were initialized with water temperature, turbidity and conductivity measurements from the May CTD profile at Station C2 (Fig. 1b).

By using a two-dimensional (2D) laterally averaged model, we assume that variations in all computed variables in the transverse direction are small compared to those in the longitudinal direction. This assumption is often used for long and narrow waterbodies like Carpenter Reservoir, which has an aspect ratio of 50:1 (Fig. 1a,b). Using a 2D model instead of a 3D model greatly reduced the computational cost and allowed us to explore a range of scenarios over a seasonal timescale. However, 2D models can have several limitations. For one, they assume symmetry in the reservoir cross-section, which is not the case in reservoirs with complex bathymetry. For example, in dendritic

or meandering reservoirs, three-dimensional effects can be important [6]. A second limitation is they ignore the effect of the Earth's rotation; for larger or wider waterbodies, the lateral transport induced by Coriolis can become important [4, 7]. Third, near-field processes such as river inflows that disperse laterally upon plunging cannot be resolved [8, 9]. Finally, 2D models can be less accurate in predicting the travel time of density currents than 3D models [10, 11].

S2 Model calibration

CE-QUAL-W2 (Version 3.72) has a number of adjustable parameters, and the parameter names used herein are the same as in the user manual [1]. We set as many parameters as possible to the default values given in the user manual. Where appropriate, parameters were determined from the observations. These and other selected parameters are summarized in Table S1.

The model was calibrated by adjusting a subset of parameters until the computed results best matched the field observations in 2015 and 2016. We evaluated the performance of the model based on two goodness-of-fit statistics: the mean bias error (MBE) and the root mean square error (RMSE). MBE is the average difference between the modelled values and measured data and is a measure of model bias. RMSE is the square root of the mean of the squared differences between the modelled values and measured data and is a measure of model accuracy.

The first step in the model calibration was a comparison of the measured and modelled water temperature, followed by conductivity, and finally turbidity. For temperature from the mooring, the measured data were compared to the model data from grid cells at the location of the mooring over time. For the CTD profiles, the measured temperature, conductivity and turbidity data were compared to the grid cells at the given station and at the time of the CTD profile. Values of MBE and RMSE for water temperature, conductivity and turbidity are given in Table S2.

S2.1 Water temperature

Water temperature in a reservoir is controlled by a variety of factors, including inflows, outflows, heat exchange at the air-water and sediment-water interfaces, solar radiation, light extinction, and mixing processes within the reservoir. As a result, to accurately model the variation in water temperature within a reservoir, a detailed set of hydrological and meteorological field data are needed to provide initial conditions, boundary conditions, and for model calibration.

The most common model parameter to be adjusted is the wind sheltering coefficient WSC. This parameter adjusts both for differences in wind from shore to water and for variations in wind along the reservoir, and the surface temperature in the model is sensitive to this value. Note the model for Carpenter Reservoir used the wind from a single land-based station, Five Mile, located near the upstream end of the reservoir (MET 1, Fig. 1b). The model was run varying WSC from 0.5 to 1.0 and a value of 0.9 produced the closest match to the observed temperature data.

The surface water temperature was also found to be sensitive to the wind-speed dependence of the evaporation function $f(W)$. This is consistent with the CE-QUAL-W2 user manual, which noted that '*the most uncertain*

parameter in the surface heat exchange computations is the evaporative wind speed function $f(W)$' [1, p. A-111], and that the coefficients of this function depend on the size and shape of the water body, as well as the location of the wind measurements. For Carpenter Reservoir the default function was chosen, $f(W) = \mathrm{AFW} + \mathrm{BFW} \times W^{\mathrm{CFW}}$, and the coefficients of this function were adjusted to provide a better match between the measured and modelled surface temperature (Table S1). Similar adjustments were used in other studies (e.g. Bonalumi et al. [3], Kobler et al. [12]).

Modelled water temperature in Carpenter Reservoir was compared to two sets of field data: (1) moored data from the thermistor chain at Station C2 near the dam and (2) vertical profiles from the monthly CTD surveys at Stations C1 to C9. The moored and modelled data were in good agreement in both 2015 (RMSE 0.88 °C) and 2016 (RMSE 1.3 °C). The RMSE was computed using model results at 3-hr intervals at the same depths as the instruments tied to the mooring; examples from six depths are shown in Fig. S2.

The modelled temperature showed similar agreement when compared to the CTD profiles in 2015 (RMSE 0.80 °C) and 2016 (RMSE 0.77 °C), see Figs. S3 and S4. The agreement between measured and modelled water temperature for Carpenter Reservoir is comparable to those reported in similar model studies (RMSEs: 0.89 °C, Gelda et al. [4]; 0.93 °C, Kobler et al. [12]; 0.61 °C, Mi et al. [13]; 0.56 °C, Ishikawa et al. [14]). Differences between the observations and the model were greatest in the thermocline because of strong vertical gradients. Other than the thermocline, the largest differences occurred in June and early July 2016 (Fig. S11d), when the total outflow from the reservoir was exceptionally high (Fig. S9b).

S2.2 Conductivity

Conductivity is a useful tracer for determining the origin of water and for estimating the exchange between water masses. The total dissolved solids (TDS) state variable was used for conductivity; variation in conductivity had a negligible contribution to density [15]. Modelled profiles of conductivity are compared to the monthly CTD casts at Stations C1 to C9 in Figs. S5 and S6. The model results compare favorably with the field data both in 2015 (RMSE 9.1 $\mu\mathrm{S\,cm^{-1}}$) and in 2016 (RMSE 11 $\mu\mathrm{S\,cm^{-1}}$). Given the range of measured conductivity in the reservoir (70 – 110 $\mu\mathrm{S\,cm^{-1}}$), the model error is approximately 8 – 15% of the measured values. Similar agreement was obtained in Sullivan et al. [16]; while the magnitude of the RMSE was lower (2.4 – 3.1 $\mu\mathrm{S\,cm^{-1}}$), the model error was a similar proportion, approximately 5 – 10% of the measured range (27 – 47 $\mu\mathrm{S\,cm^{-1}}$).

S2.3 Turbidity

A number of factors influence the turbidity in a receiving water body, including the stratification of the water body, turbidity and plunge depth of the inflows, suspended particle size, and particle settling rate. The inorganic suspended solids (ISS) state variable was used for turbidity, and variations in turbidity had a negligible contribution to density [15]. During model calibration, the particle settling velocity was adjusted to best match the field data. A settling velocity of $\mathrm{SSS} = 0.2\ \mathrm{m\,d^{-1}}$ was selected (Table S1), which corresponds to Stokes settling of particles with a diameter of $\sim$2 µm. Suspended particles in Carpenter Reservoir have a range of sizes and settling rates; they do not settle under the idealized conditions assumed by Stokes' law (dilute suspensions of spherical particles

in a quiescent fluid), and flocculation may also play a role [17, 18]. Therefore, the selected settling rate is not intended to represent a single particle size; rather, it represents the best fit to the distribution of particles giving rise to turbidity in Carpenter Reservoir.

Modelled turbidity profiles are compared to monthly CTD casts at Stations C1 to C9 in Figs. S7 and S8. Modelled turbidity agrees favorably with measurements in both 2015 (RMSE 5.7 NTU) and 2016 (RMSE 7.1 NTU). Given the range of measured turbidity in the reservoir (0 – 40 NTU), the model error is approximately 15% of the measured values. Similar agreement was obtained in Sullivan et al. [16]; while the magnitude of the RMSE was lower (0.7 NTU), the model error was a similar proportion, approximately 11 – 12%, of the measured range (0 – 6 NTU). Note that the RMSE values include both the epilimnion where turbidity is generally low and the hypolimnion where turbidity is high and variable. Restricting the comparison to 0 – 3 m, representative of the epilimnion, gave for 2015 an RMSE of 1.7 NTU and for 2016 an RMSE of 1.9 NTU.

S2.4 Effect of initial conditions

The simulations began from rest with the initial temperature, conductivity, and turbidity set to the vertical profile collected at Station C2. That is, the initial velocity was zero and the initial scalars varied in the vertical direction, but not in the horizontal direction. This meant that a time was required for densities, velocities, and scalars to come into equilibrium, namely a spin-up period. The simulated temperature was found to be similar to the moored temperature after an initial spin-up period of 5 days, consistent with the spin-up periods found in other modelling studies (2 d, Rueda and Schladow [19]; 3 d, Rueda et al. [20]; 5 d, Valbuena. et al. [21]).

S2.5 Effect of grid resolution

The effect of grid resolution was tested by increasing the number of horizontal segments until further increases did not significantly change the simulated results. The model was run using 15, 33, 56, and 105 horizontal segments, with errors expressed as the relative L2 norm error between the simulated results at different grid resolutions and those using the highest grid resolution [e.g. 22, 23]. For the 2015 model run, errors in temperature using the 56-segment grid were less than 2%. As a result, this horizontal grid resolution was selected for all simulations.

A vertical grid resolution of 0.5 m was chosen based on guidance from the user manual, which provides examples with layer thicknesses ranging from 0.3 to 2 m [1], and from previous studies of similar water bodies, in which layer thicknesses ranged from 0.5 to 2 m (2 m, Bonalumi et al. [3]; 1 m, Gelda et al. [4]; 0.5 m, Kobler et al. [12]).

S3 Additional model results

S3.1 Modelled seasonal stratification in 2016

The modelled temperature, turbidity and conductivity were shown in Fig. 2 for 2015 and are here shown for 2016 in Fig. S9. In 2015, there was a period with particularly warm air and water temperature in early July (Fig. 2d,h), while in 2016, the warmest periods occurred in late July and early August (Fig. S9d,h). The modelled turbidity

in the epilimnion declined through the summer (Fig. S9i) while the conductivity in the epilimnion increased (Fig. S9j).

S3.2 Model tracers

Passive conservative tracers were simulated to track the fraction of water originating from different sources, namely the fraction of water in the reservoir that was: (1) initial water in the reservoir at the beginning of the model run, (2) inflow from La Joie Dam and (3) inflow from the local tributaries, all at Station C2. At each depth and for each time, the sum of the values of these three tracers is equal to one.

At the beginning of the model run, on 22 May 2015, the entire water column was occupied by the initial water in the reservoir (Fig. S10b). After $\sim$10 days, much of the initial water below 20 m was replaced by water from the inflows, and by July 2015, nearly all the initial water in the hypolimnion had been flushed. By contrast, an appreciable fraction of the initial water in the epilimnion remained for most of the summer. In September 2015, the epilimnion began to deepen adding water from below, and the fraction of original water in the epilimnion began to decrease more rapidly (Fig. S10b). By October, much of the initial water in the epilimnion was replaced by turbid inflow, a mix of water from the local tributaries and from La Joie Dam (Fig. S10c,d). The results for 2016 were similar, except for the epilimnion in early June when a marked decrease in the original water occurred (Fig. S10f) driven by cool weather, wind and high through flow.

S3.3 Comparison of measured and modelled data in 2015 and 2016

In the epilimnion, the measured and modelled temperature, turbidity, and conductivity, along with the modelled tracers, are summarized for both 2015 and 2016 in Fig. S11. Results are shown at 1 m depth, representative of the epilimnion, and at Station C2 near the dam. In both years, the modelled temperature showed the expected seasonal cycle (Fig. S11a,b); the modelled turbidity declined from May to August (Fig. S11c,d); and the conductivity and the tracer for initial water declined through the summer (Fig. S11e–h).

There were notable differences between 2015 and 2016, particularly in spring. The storm on 10 June 2016 occurred during a period of very high outflow (Fig. S9b), and lower temperature stratification (Fig. S9h) than occurred during the same period in 2015. In effect, the storm of 10 June 2016 resulted in partial mixing of the epilimnion, and the fraction of initial water in the epilimnion dropped from close to 1 before the storm to $\sim$0.75 after the storm (Fig. S11d).

S3.4 Modelled scenarios driven by historical flows (1965 – 2017)

The model results using the inflows and outflows from 1965 to 2017, with the meteorology and tributary sampling data collected in 2016, are shown in Figs. S12 and S13. Using the meteorology and tributary sampling data collected in 2015 gave similar results, see Figs. 4 and 5.

References

[1] Cole, T.M., Wells, S.A.: CE-QUAL-W2: A two-dimensional, laterally averaged, hydrodynamic and water quality model, version 3.72. Technical report, Department of Civil and Environmental Engineering, Portland State University, Portland, Oregon (2015)

[2] Rodi, W.: Turbulence models and their application in hydraulics: A state of the art review (1980)

[3] Bonalumi, M., Anselmetti, F.S., Wüest, A., Schmid, M.: Modeling of temperature and turbidity in a natural lake and a reservoir connected by pumped-storage operations. Water Resour. Res. **48**(8), 08508 (2012) https://doi.org/10.1029/2012wr011844

[4] Gelda, R.K., King, A.T., Effler, S.W., Schweitzer, S.A., Cowen, E.A.: Testing and application of a two-dimensional hydrothermal/transport model for a long, deep, and narrow lake with moderate Burger number. Inland Waters **5**(4), 387–402 (2015) https://doi.org/10.5268/iw-5.4.804

[5] Kobler, U.G., Wüest, A., Schmid, M.: Combined effects of pumped-storage operation and climate change on thermal structure and water quality. Climatic Change **152**(3-4), 413–429 (2019) https://doi.org/10.1007/s10584-018-2340-x

[6] Chung, S.W., Hipsey, M.R., Imberger, J.: Modelling the propagation of turbid density inflows into a stratified lake: Daecheong Reservoir, Korea. Environ. Model. Softw. **24**(12), 1467–1482 (2009) https://doi.org/10.1016/j.envsoft.2009.05.016

[7] Boegman, L., Loewen, M.R., Hamblin, P.F., Culver, D.A.: Application of a two-dimensional hydrodynamic reservoir model to Lake Erie. Can. J. Fish. Aquat. Sci. **58**(5), 858–869 (2001) https://doi.org/10.1139/f01-035

[8] Scheu, K.R., Fong, D.A., Monismith, S.G., Fringer, O.B.: Sediment transport dynamics near a river inflow in a large alpine lake. Limnol. Oceanogr. **60**(4), 1195–1211 (2015) https://doi.org/10.1002/lno.10089

[9] Scheu, K.R., Fong, D., Monismith, S.G., Fringer, O.B.: Modeling Sedimentation Dynamics of Sediment-Laden River Intrusions in a Rotationally-Influenced, Stratified Lake. Water Resour. Res. **54**(6), 4084–4107 (2018) https://doi.org/10.1029/2017wr021533

[10] Patterson, M.D., Simpson, J.E., Dalziel, S.B., Nikiforakis, N.: Numerical modelling of two-dimensional and axisymmetric gravity currents. Int. J. Numer. Meth. Fl. **47**(10-11), 1221–1227 (2005) https://doi.org/10.1002/fld.841

[11] DeCesare, G., Boillat, J.-L., Schleiss, A.J.: Circulation in stratified lakes due to flood-induced turbidity currents. J. Environ. Eng. **132**(11), 1508–1517 (2006) https://doi.org/10.1061/(asce)0733-9372(2006)132:11(1508)

[12] Kobler, U.G., Wüest, A., Schmid, M.: Effects of Lake–Reservoir Pumped-Storage Operations on Temperature and Water Quality. Sustainability **10**(6), 1968 (2018) https://doi.org/10.3390/su10061968

[13] Mi, C., Shatwell, T., Ma, J., Xu, Y., Su, F., Rinke, K.: Ensemble warming projections in Germany's largest drinking water reservoir and potential adaptation strategies. Sci. Total Environ. **748**, 141366 (2020) https://doi.org/10.1016/j.scitotenv.2020.141366

[14] Ishikawa, M., Gonzalez, W., Golyjeswski, O., Sales, G., Rigotti, J.A., Bleninger, T., Mannich, M., Lorke, A.: Effects of dimensionality on the performance of hydrodynamic models for stratified lakes and reservoirs. Geosci. Model Dev. **15**(5), 2197–2220 (2022) https://doi.org/10.5194/gmd-15-2197-2022

[15] Robb, D.M., Pieters, R., Lawrence, G.A.: Fate of turbid glacial inflows in a hydroelectric reservoir. Environ. Fluid Mech. **21**, 1201–1225 (2021) https://doi.org/10.1007/s10652-021-09815-4

[16] Sullivan, A.B., Rounds, S.A., Sobieszczyk, S., Bragg, H.M.: Modeling hydrodynamics, water temperature, and suspended sediment in Detroit Lake, Oregon. Technical report, U. S. Geological Survey (2007)

[17] Hodder, K.R., Gilbert, R.: Evidence for flocculation in glacier-fed Lillooet Lake, British Columbia. Water Res. **41**(12), 2748–2762 (2007) https://doi.org/10.1016/j.watres.2007.02.058

[18] Hodder, K.R.: Flocculation: a key process in the sediment flux of a large, glacier-fed lake. Earth Surf. Proc. Land. **34**(8), 1151–1163 (2009) https://doi.org/10.1002/esp.1807

[19] Rueda, F.J., Schladow, S.G.: Dynamics of Large Polymictic Lake. II: Numerical Simulations. J. Hydraul. Eng. **129**(2), 92–101 (2003) https://doi.org/10.1061/(asce)0733-9429(2003)129:2(92)

[20] Rueda, F., Vidal, J., Schladow, G.: Modeling the effect of size reduction on the stratification of a large wind-driven lake using an uncertainty-based approach. Water Resour. Res. **45**(3), 03411 (2009) https://doi.org/10.1029/2008wr006988

[21] Valbuena., S.A., Bombardelli, F.A., Cortés, A., Largier, J.L., Roberts, D.C., Forrest, A.L., Schladow, S.G.: 3D flow structures during upwelling events in lakes of moderate size. Water Resour. Res. **58**, 030666 (2022) https://doi.org/10.1029/2021wr030666

[22] Fringer, O.B., Gerritsen, M., Street, R.L.: An unstructured-grid, finite-volume, nonhydrostatic, parallel coastal ocean simulator. Ocean Model. **14**, 139–173 (2006) https://doi.org/10.1016/j.ocemod.2006.03.006

[23] Ramón, C.L., Ulloa, H.N., Doda, T., Bouffard, D.: Flushing the Lake Littoral Region: The Interaction of Differential Cooling and Mild Winds. Water Resour. Res. **58**(3), 030943 (2022) https://doi.org/10.1029/2021wr030943

Table S1 Model parameters used in this study and the default CE-QUAL-W2 values. The column on the right indicates whether the parameters were based on field observations (obs), selected as calibration parameters (cal), or set to default values (def).

Parameter	Description	Value	Default	Based on
Inorganic suspended solids				
SSS	Settling velocity ($m\,day^{-1}$)	0.2	1	cal
SEDRC	Sediment resuspension	OFF	OFF	def
Mixing parameters				
FRICT	Chezy coefficient ($m^{0.5}\,s^{-1}$)	70	70	def
AX	Longitudinal eddy viscosity ($m^2\,s^{-1}$)	1	1	def
DX	Longitudinal eddy diffusivity ($m^2\,s^{-1}$)	1	1	def
AZMAX	Maximum vertical eddy viscosity ($m^2\,s^{-1}$)	1	1	def
FI	Internal friction coefficient (-)	0.015	0.015	def
Scaling of meteorological forcing				
SHD	Shading coefficient (-)	1	1	def
WSC	Wind sheltering coefficient (-)	0.9	1	cal
Heat exchange at air-water interface coefficients				
AFW	Wind function coefficient ($W\,m^{-2}mm\,Hg^{-1}$)	5.0	9.2	cal
BFW	Wind function coefficient ($W\,m^{-2}mm\,Hg^{-1}(m\,s^{-1})^{-CFW}$)	7.2	0.46	cal
CFW	Wind function coefficient (-)	1	2	cal
Heat exchange at sediment-water interface				
TSED	Sediment temperature (°C)	11.9	-	obs
CBHE	Coeff. of bottom heat exchange ($W\,m^{-2}\,°C$)	0.3	0.3	def
Light attenuation in water column				
EXH20	Light extinction coeff. of water and dissolved substances (m^{-1})	0.185	0.25	obs
EXSS	Turbidity-specific light extinction coeff. ($m^{-1}\,NTU^{-1}$)	0.081	0.1	obs
BETA	Fraction of solar radiation absorbed at water surface (-)	0.45	0.45	def

Table S2 Mean bias error (MBE) and root mean square error (RMSE) of temperature, conductivity, and turbidity. Model results were compared to field measurements from the temperature mooring and the vertical profiles from the monthly surveys.

Measurement	**Variable**	**Unit**	**Mean Bias Error**		**RMSE**	
			Year 2015	**Year 2016**	**Year 2015**	**Year 2016**
Mooring	Temperature	°C	−0.32	−0.20	0.88	1.3
Profiles	Temperature	°C	0.05	−0.26	0.80	0.77
	Conductivity	$\mu S\,cm^{-1}$	−0.29	−6.4	9.1	11
	Turbidity	NTU	0.65	3.6	5.7	7.1

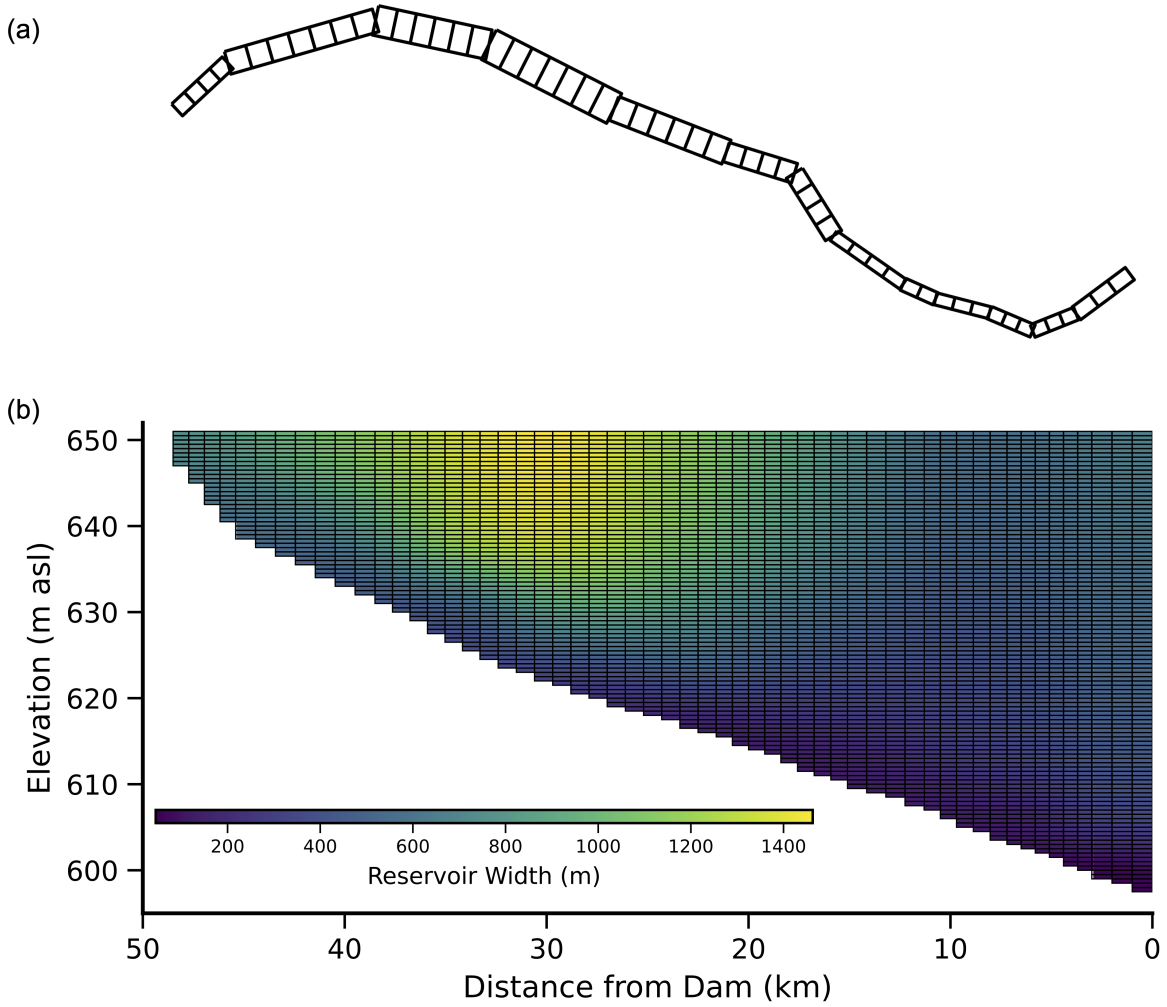

Fig. S1 (a) Plan view and (b) side view of the model grid. In (b), the contours indicate the width, in the lateral direction, of each grid cell.

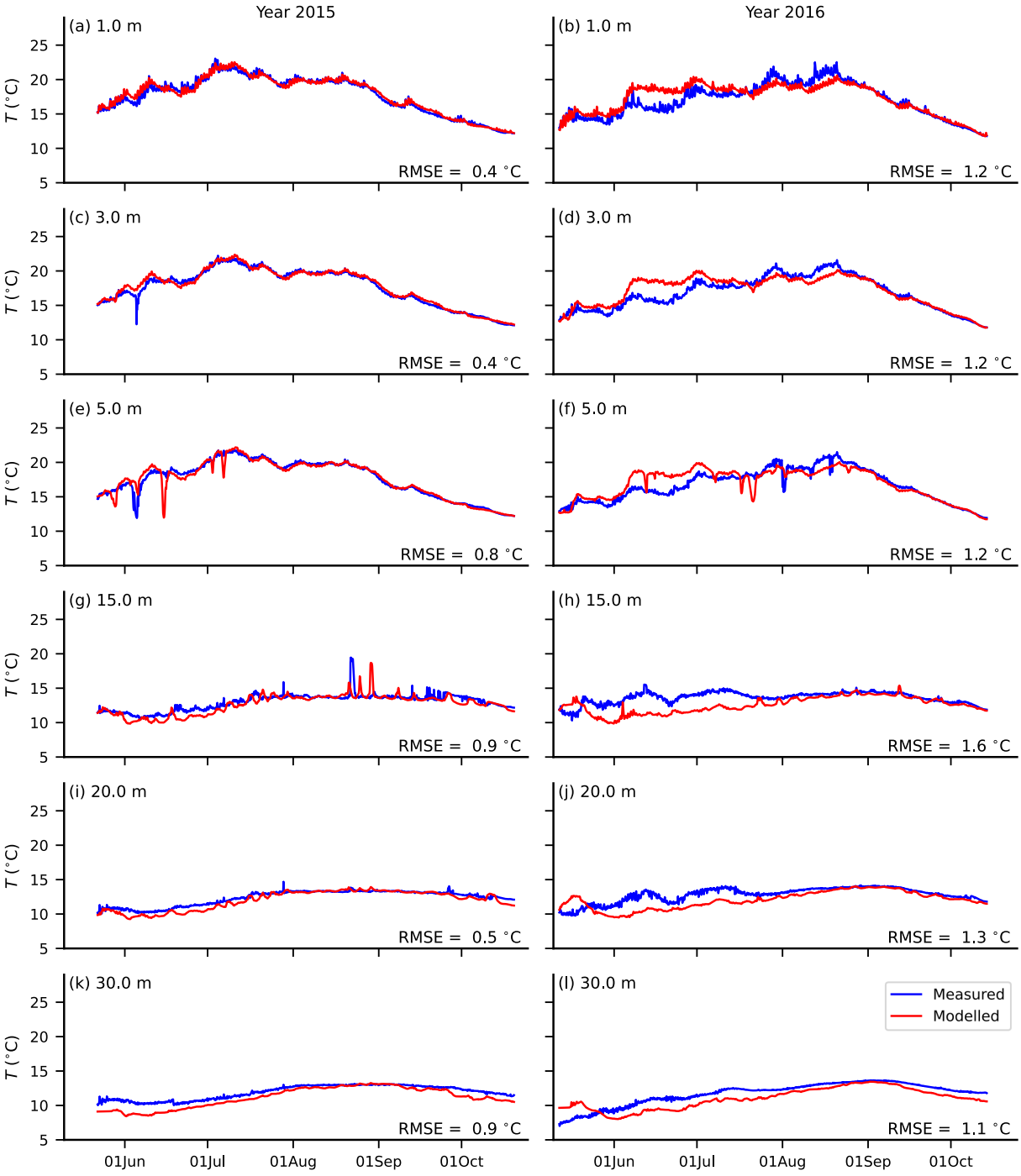

Fig. S2 Measured and modelled water temperature at Station C2 at selected depths. Year 2015 (left) and 2016 (right).

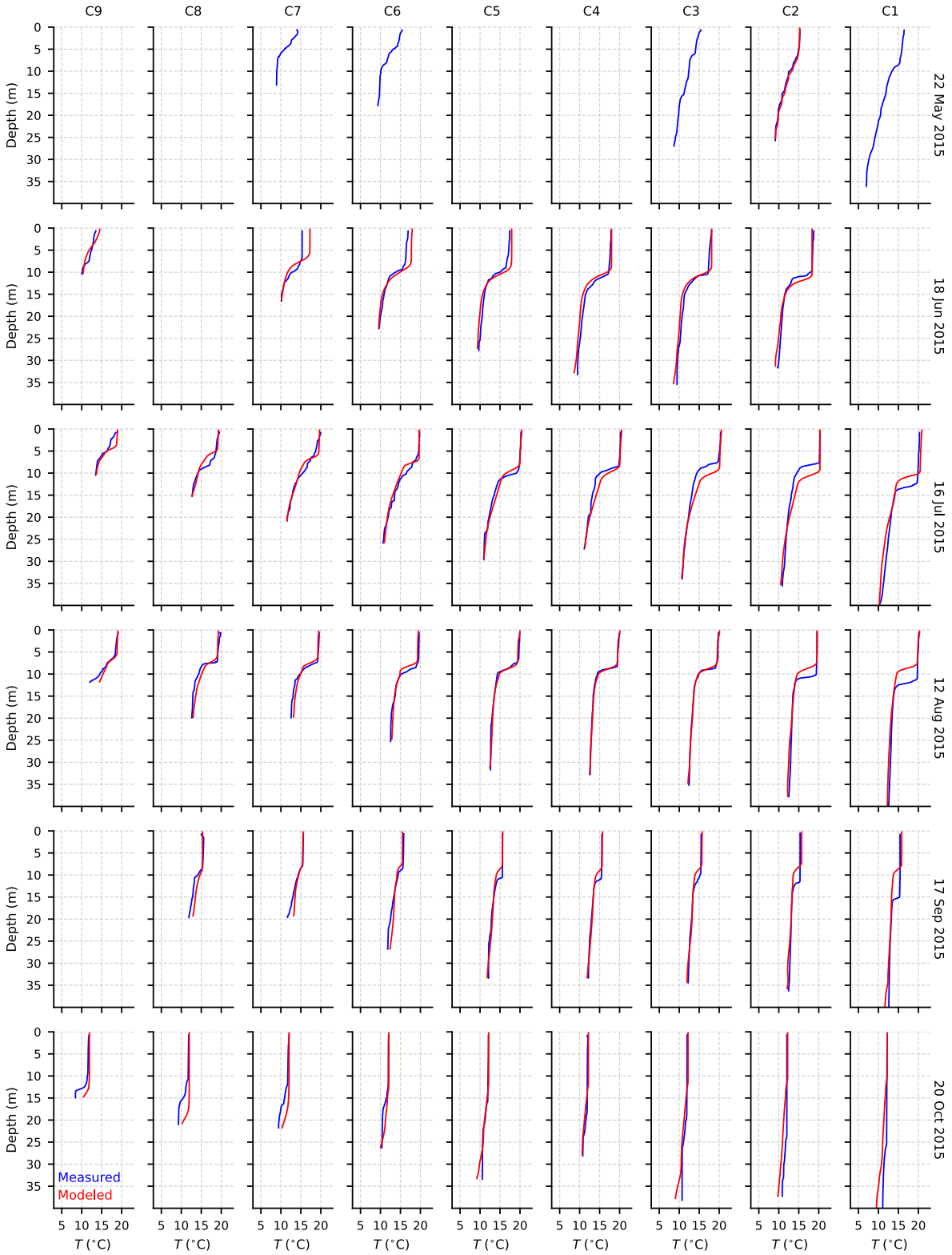

Fig. S3 Measured and modelled temperature profiles at Stations C1 – C9 in 2015. Blank panels mark casts not collected. Data from the first profile at Station C2 was used as the initial condition for the model along the whole reservoir.

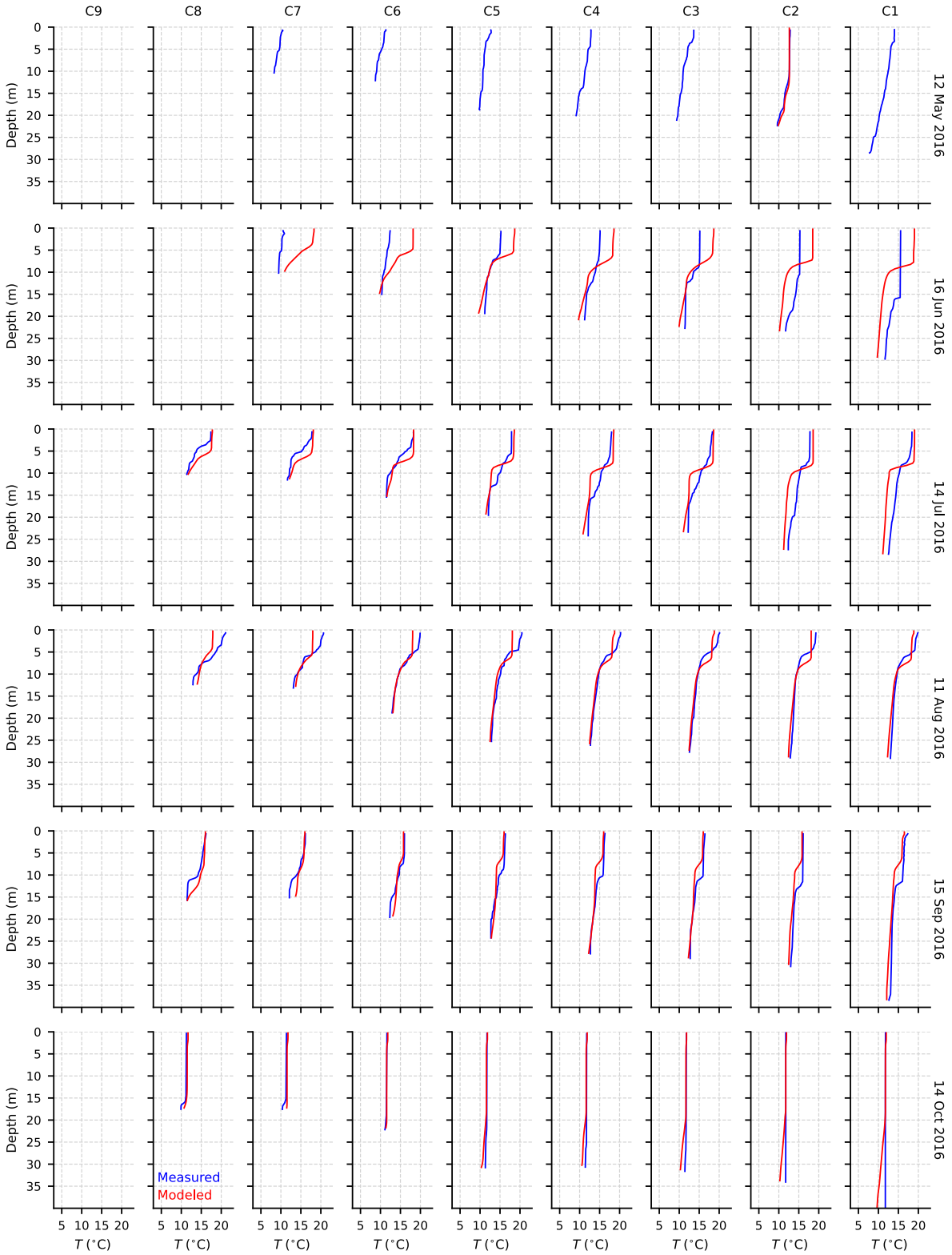

Fig. S4 Measured and modelled temperature profiles at Stations C1 – C9 in 2016. Blank panels mark casts not collected. Data from the first profile at Station C2 was used as the initial condition for the model along the whole reservoir.

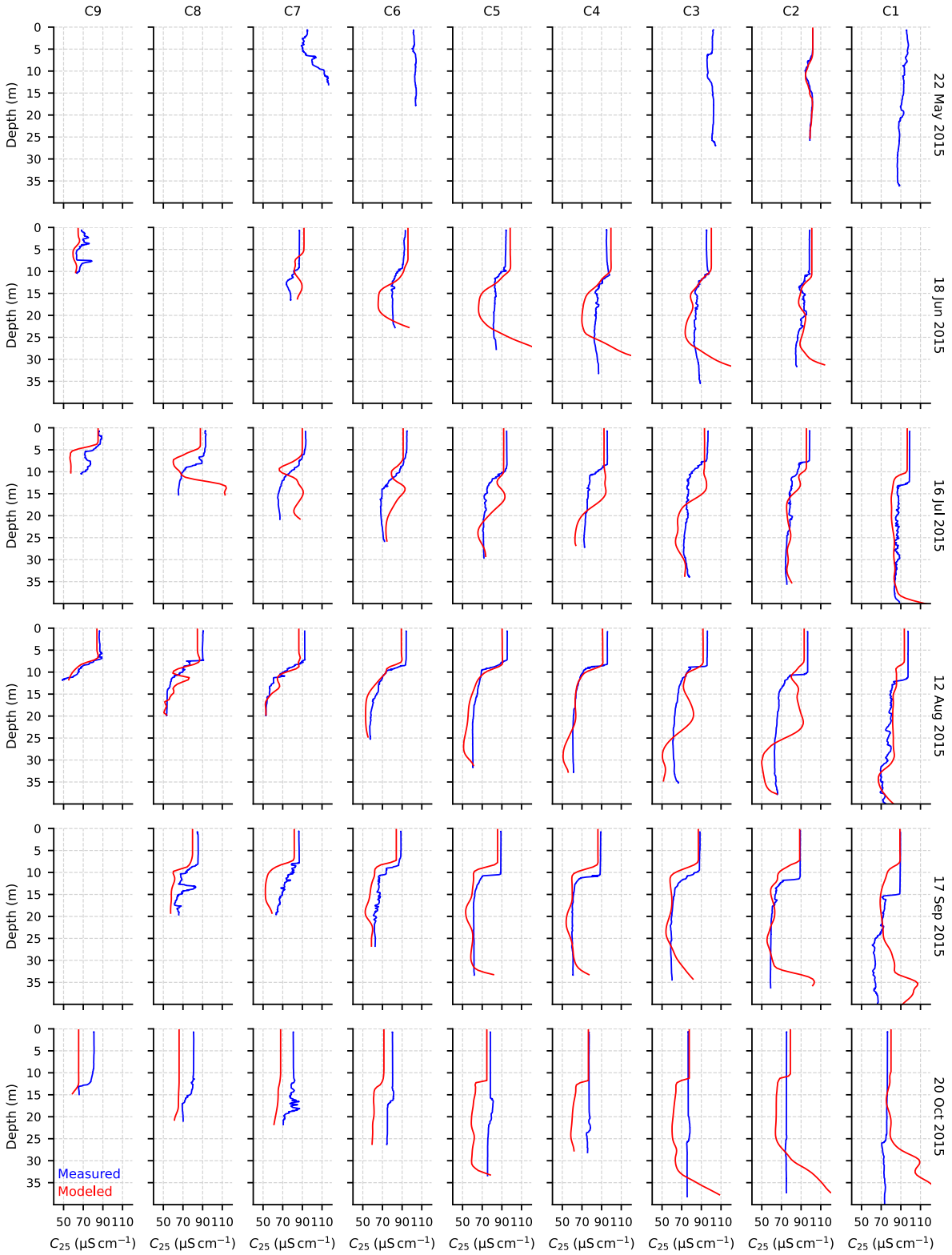

Fig. S5 Measured and modelled conductivity profiles at Stations C1 – C9 in 2015. Blank panels mark casts not collected. Data from the first profile at Station C2 was used as the initial condition for the model along the whole reservoir.

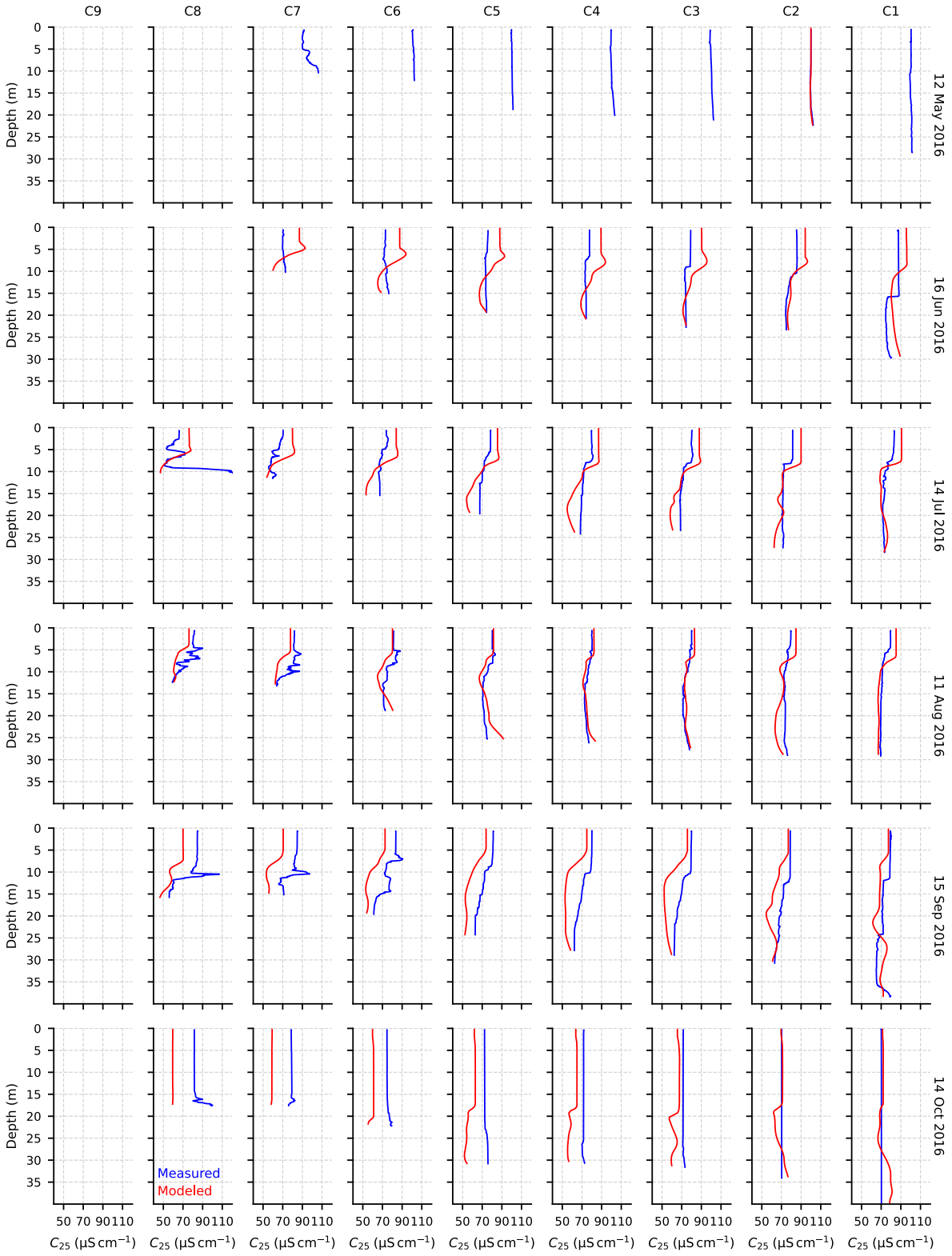

Fig. S6 Measured and modelled conductivity profiles at Stations C1 – C9 in 2016. Blank panels mark casts not collected. Data from the first profile at Station C2 was used as the initial condition for the model along the whole reservoir.

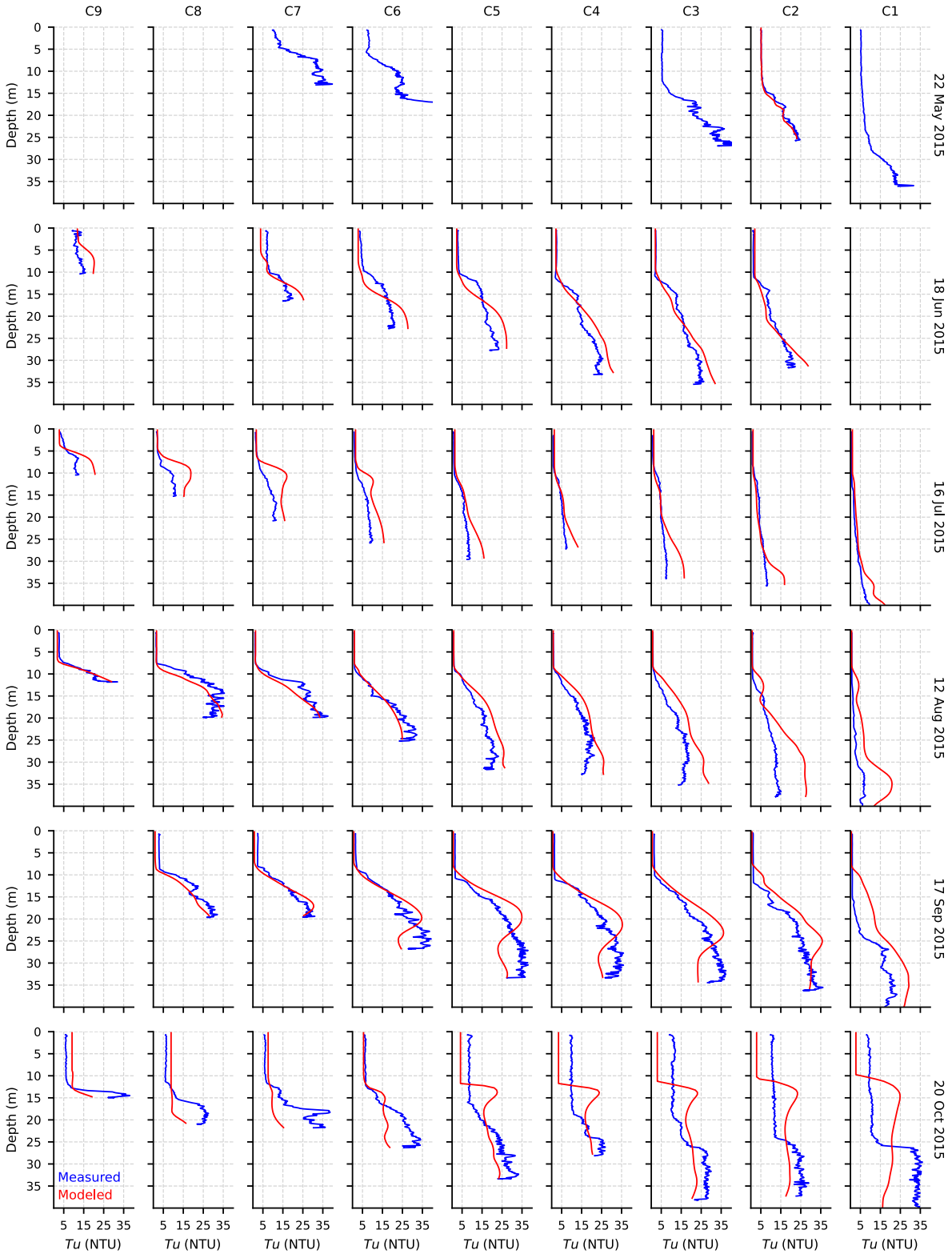

Fig. S7 Measured and modelled turbidity profiles at Stations C1 – C9 in 2015. Blank panels mark casts not collected. Data from the first profile at Station C2 was used as the initial condition for the model along the whole reservoir.

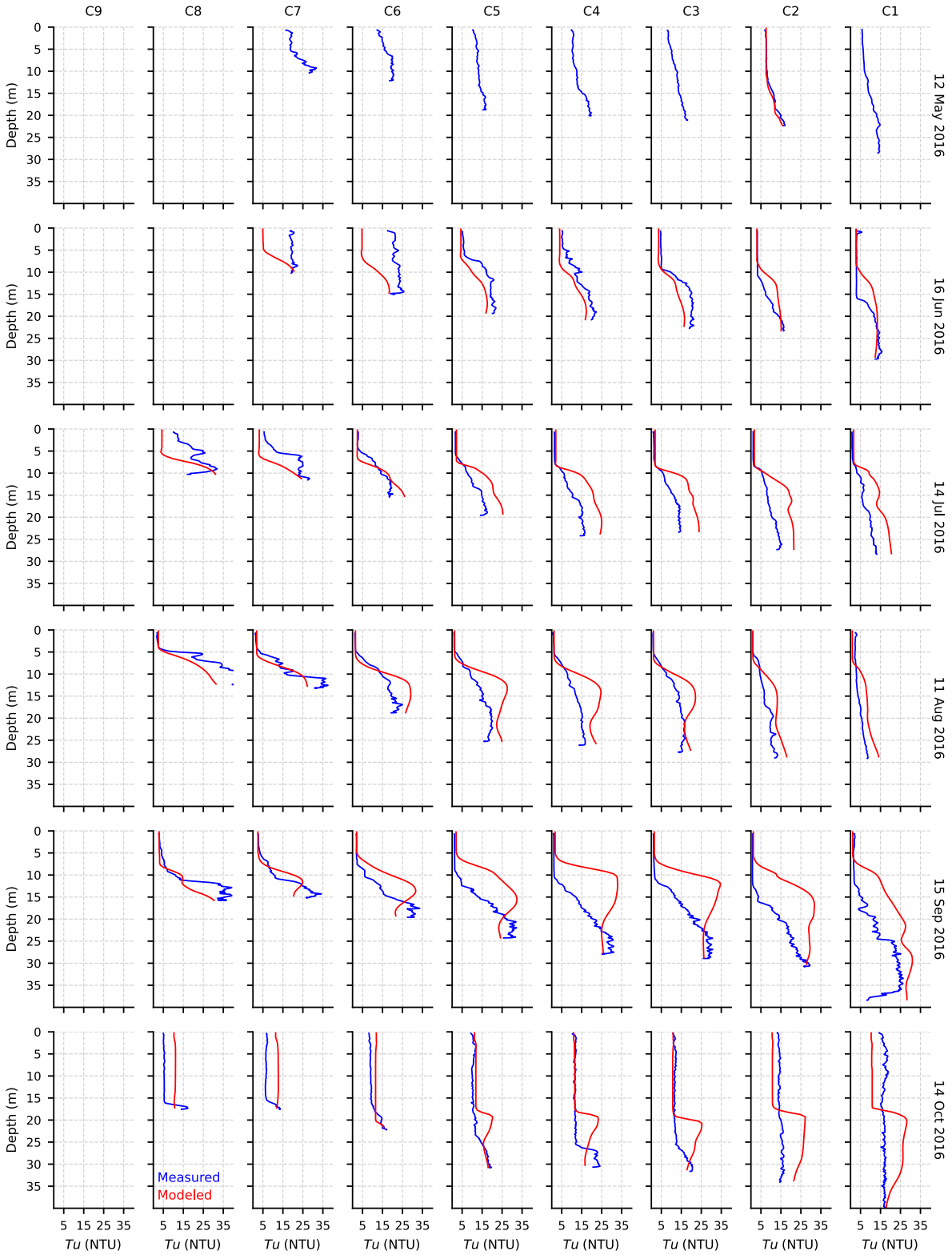

Fig. S8 Measured and modelled turbidity profiles at Stations C1 – C9 in 2016. Blank panels mark casts not collected. Data from the first profile at Station C2 was used as the initial condition for the model along the whole reservoir.

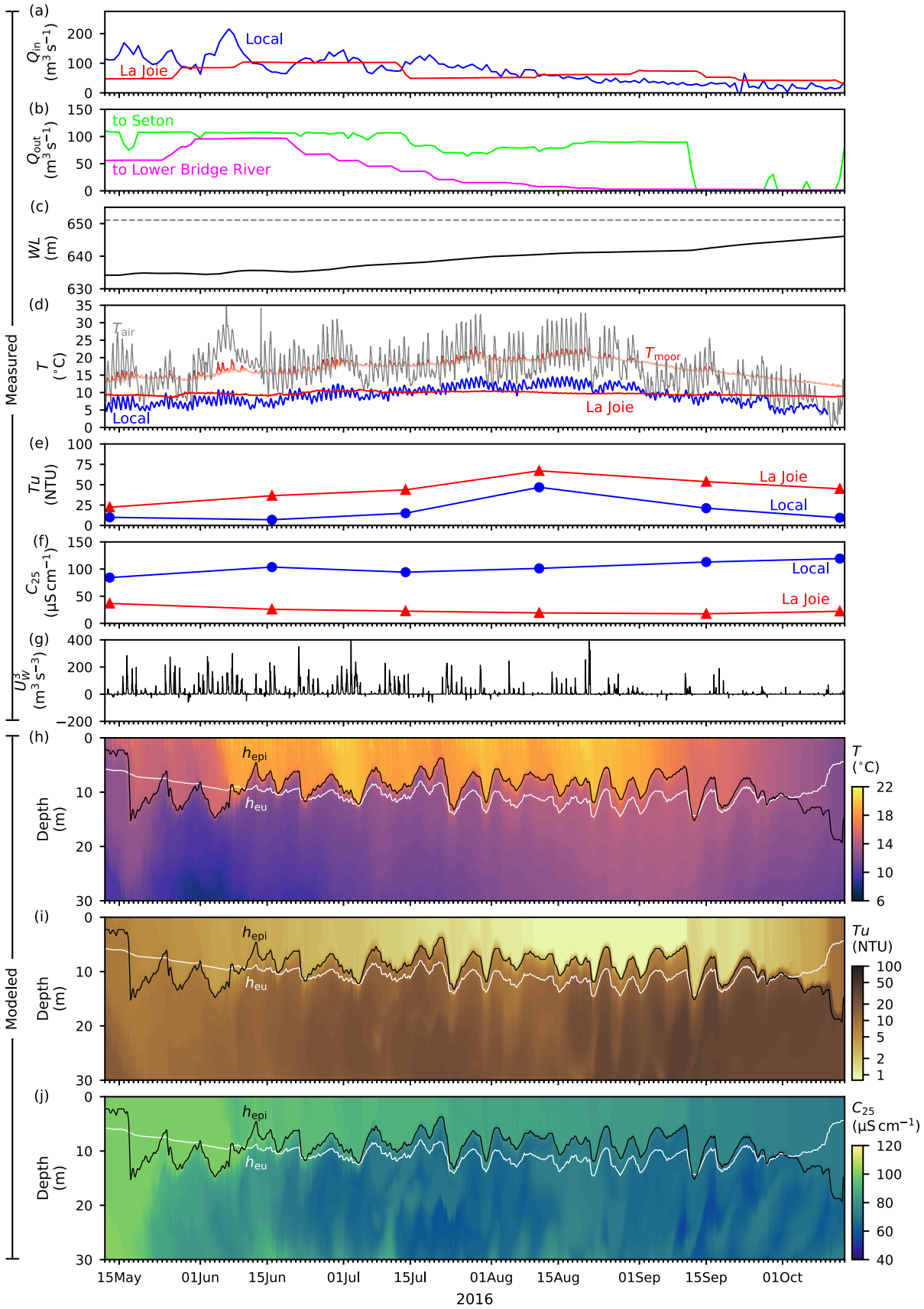

Fig. S9 Measured (a) inflows, (b) outflows, (c) water level, (d–f) flow-weighted tributary temperature, turbidity and conductivity, (g) along-axis wind speed cubed; and modelled (h–j) temperature, turbidity and conductivity, at Station C2, 12 May to 14 October 2016. In (c), the dashed line marks full pool (651.08 m asl). In (d), air temperature and mooring temperature (0–5 m) are shown in grey and shades of red. In (g), positive wind is from the west toward the dam. In (h–j), the black line marks the epilimnion depth (maximum temperature gradient) and the white line the euphotic depth.

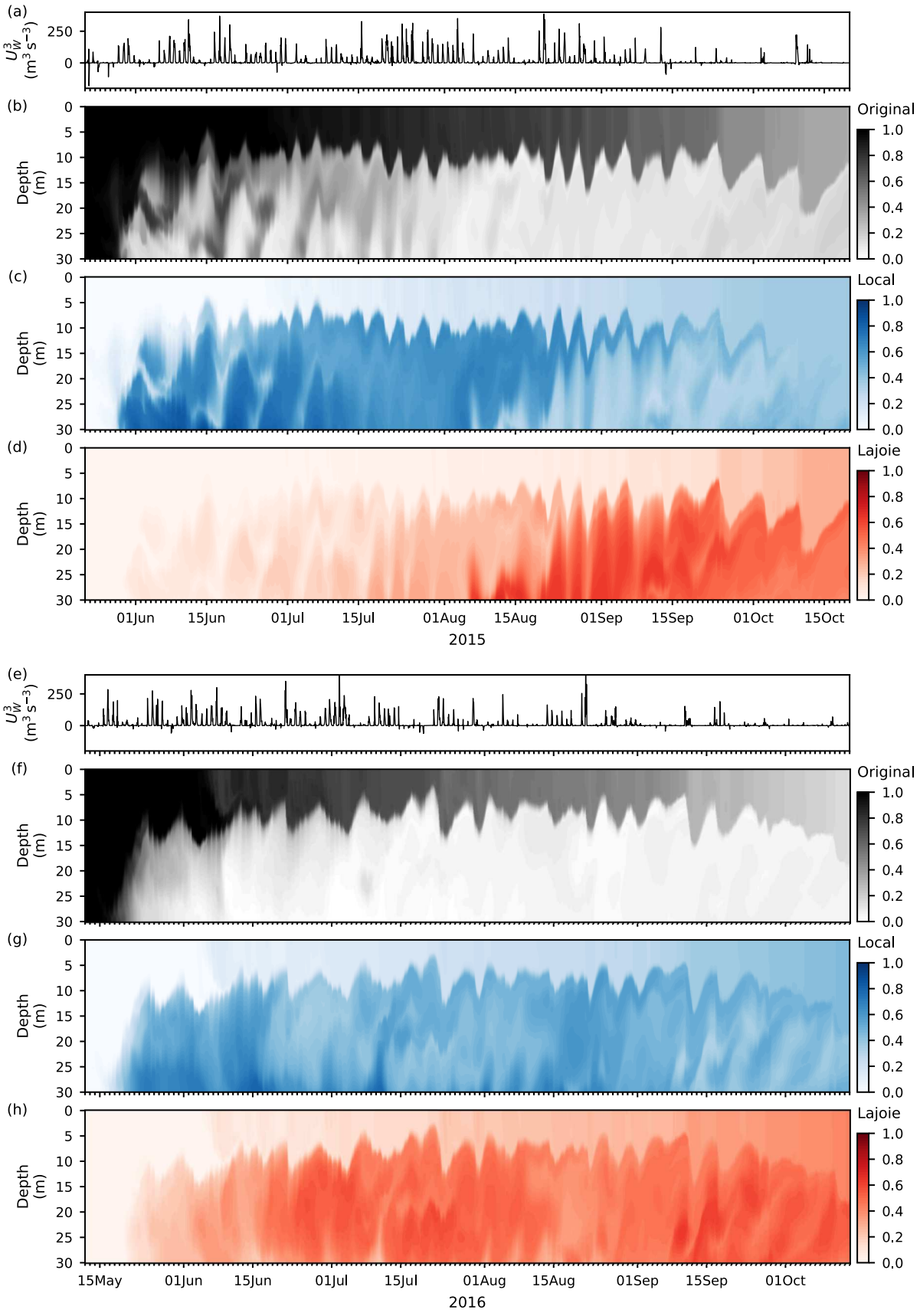

Fig. S10 Time series of observed along-axis wind speed cubed and simulated tracers from (a–d) 22 May to 20 October 2015 and (e–h) 12 May to 14 October 2016. In (a, e), positive wind is from the west toward the dam. Tracers represent (b, f) the original water in the reservoir at the beginning of the model run, (c, g) the inflow from the local tributaries, and (d, h) the inflow from La Joie Dam.

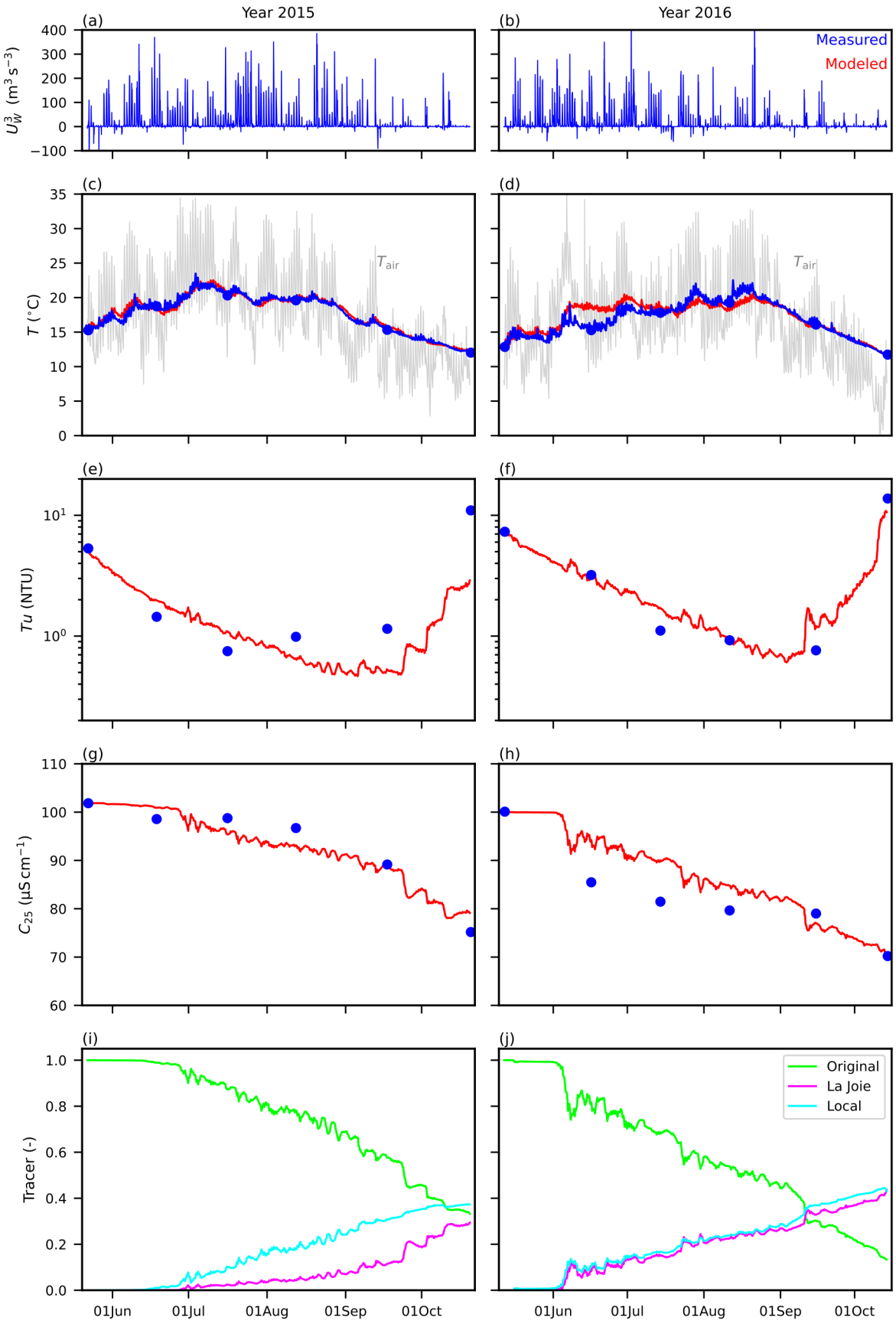

Fig. S11 (a, b) Measured along-axis wind speed cubed. Comparison of measured and modelled (c, d) temperature, (e, f) turbidity, and (g, h) conductivity in (left) 2015 and (right) 2016. (i, j) Modelled tracer concentrations. Both the measured and modelled data were from Station C2 at 1 m depth.

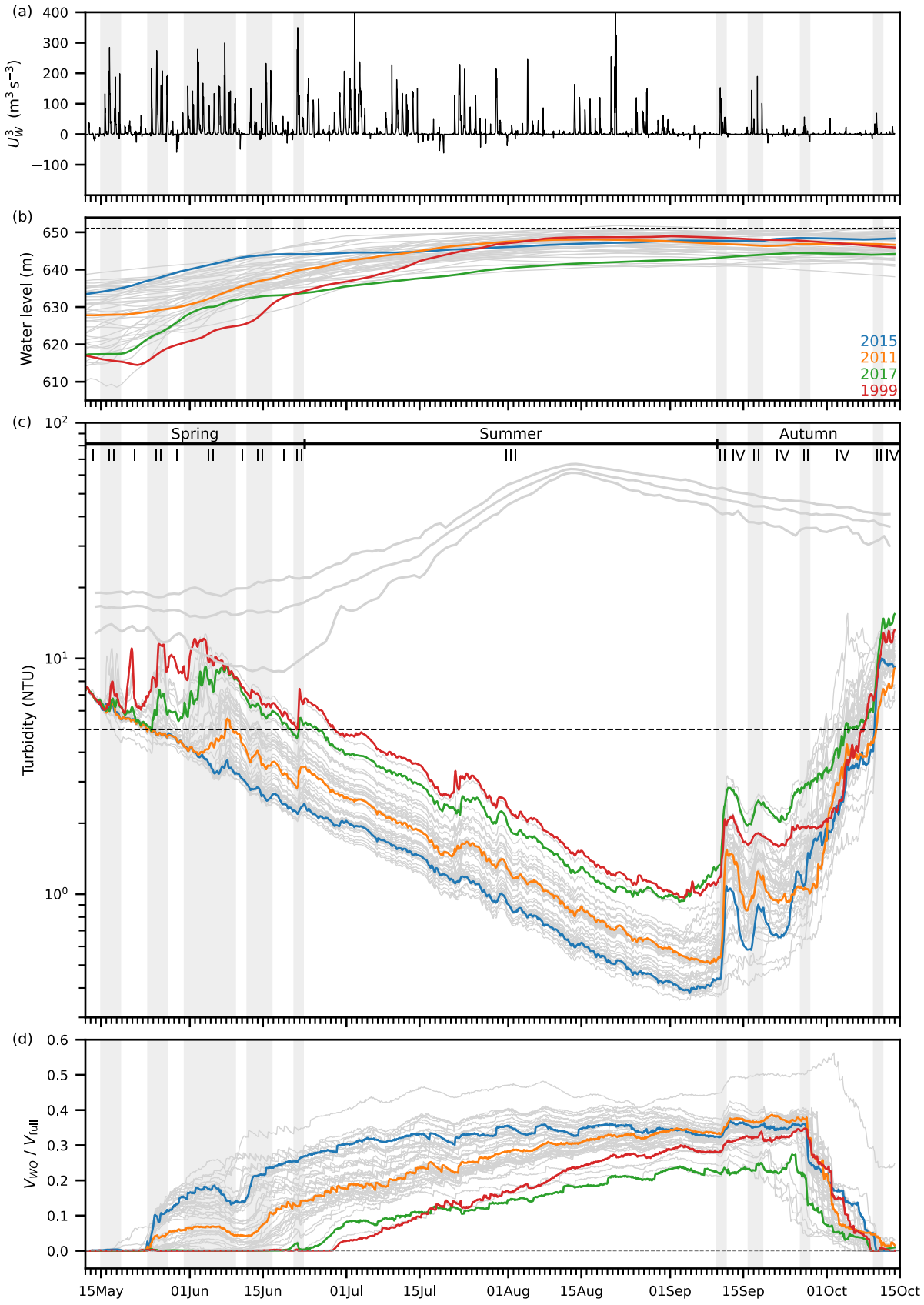

Fig. S12 Time series of (a) observed along-axis wind speed cubed, and (b) simulated reservoir water level, (c) simulated turbidity at Station C2 at 1 m depth, and (d) simulated volume of the reservoir with a turbidity less than 5 NTU divided by the reservoir volume at full pool (651.08 m asl, 1.0×10^9 m^3). In (a), positive wind speed is from the west toward the dam. In (b), the dashed line marks the elevation of full pool. In (b–d), the thin grey lines show the model results for all years 1965 – 2017, and the coloured lines show selected years. In (c), the thick grey lines show the flow-weighted turbidity of the inflows (median, 5th and 95th percentile). All model runs use the meteorological and tributary sampling data from 2016 (using 2015 gave similar results, see Fig. 4). Roman numerals mark Regimes described in the text.

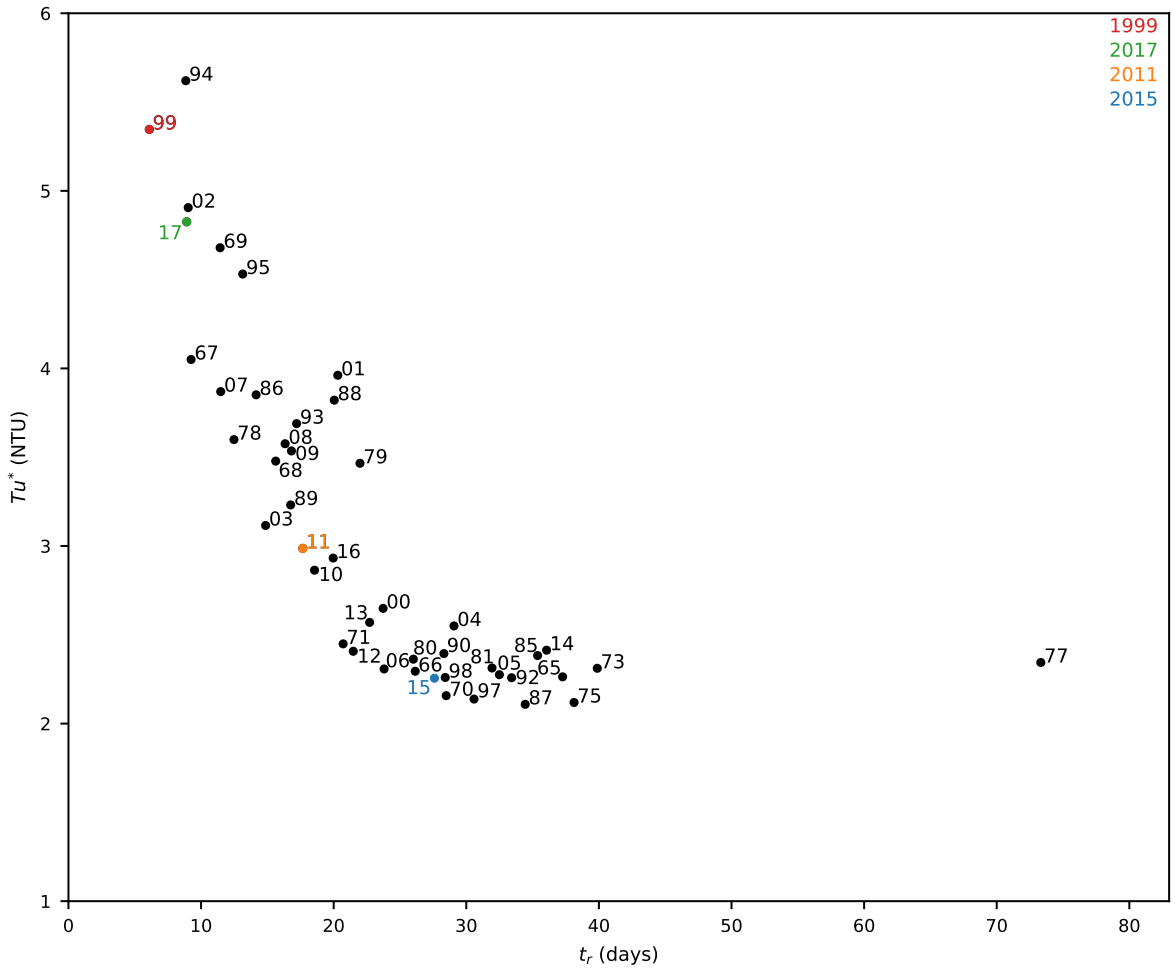

Fig. S13 Relationship between epilimnetic turbidity at Station C2 at 1 m depth at the beginning of summer, Tu^*, and the average residence time from the beginning of the model run to the beginning of summer, t_r, (22 May – 20 June). Shown are model runs (1965 – 2017) using the meteorological and tributary sampling data from 2016 (using 2015 gave similar results, see Fig. 5).